APPLICATION OF DIAMETRAL COMPRESSION TEST TO EVALUATION OF DENTIN-ADHESIVE INTERFACE BOND STRENGTH

By

Rizacan Sarikaya

Submitted to the graduate degree program in Mechanical Engineering and the Graduate Faculty of University of Kansas in partial fulfillment of the requirements for the degree of Master of Science

Chairperson _____ Dr. Anil Misra

Committee Members _____ Dr. Paulette Spencer

_____ Dr. Candan Tamerler

Date Defended: Aug 15, 2017

The Thesis Committee for Rizacan Sarikaya certifies

that this is the approved version of the following thesis:

APPLICATION OF DIAMETRAL COMPRESSION TEST TO EVALUATION OF DENTIN-ADHESIVE INTERFACE BOND STRENGTH

_____

Dr. Anil Misra, Chairperson

Date Approved: Aug 15, 2017

Abstract

Bond strength test is crucial for evaluation of dentin-adhesive effectiveness and for informing the design of adhesive systems. Conventional bond strength techniques have limitations with respect to accuracy and suffer from large variability. Diametral compression test is an alternative approach for evaluating bond strength which aims to simplify the boundary conditions during loading. For the dentin-adhesive interface, this type of test can be applied to not only access the tensile behavior but also behavior under complex combined normal and shear loading conditions.

With an aim to design laboratory experiments, extensive finite element analyses are carried out on diametral compression test. The performed analyses utilize a novel granular micromechanics based user-defined nonlinear material model that has been implemented into commercial finite element analysis software. Failure evolution and debonding are investigated for FE models with varying geometries, materials and interface properties.

Results of this numerical study shows that failure mode can be controlled by changing the design of diametral compression disc samples and accordingly, accuracy of bond strength test can be improved. Furthermore, diametral compression test can provide tensile and shear bond strength test using a single test setup changing interface orientation of a bilayered disc specimen.

Acknowledgements

I would like to express my gratitude to Dr. Anil Misra, Dr. Paulette Spencer and Dr. Candan Tamerler for their constant support, invaluable supervision, precious guidence and giving me the opportunity to be a part of their research group and work on this project.

I would also like to thank all my colleagues working on the same project with me for their contributions in providing different perspectives during our research meetings.

I also gratefully acknowledge support for this work from the National Institutes of Health, grant number: NIH/NIGMS/NIDCR 1R01DE025476.

Finally, I would like to thank my family for their emotional support, infinite love and encouragement they provided me all my life.

Table of Contents

List of figures

List of Tables

CHAPTER 1

INTRODUCTION, LITERATURE REVIEW AND SCOPE OF WORK

1.1 INTRODUCTION

Restorative dentistry has potential for further development considering failure rates reported in 2005 such as more than 83 million of the 166 million dental restorations placed in the United States where 77 million of total dental restorations were resin composites whose lifespan is restricted such as 5 to 8 years [1-4].

Accurate evaluation of mechanical properties provides better insights in order to create an effective design of restorative materials. Desired properties can be accurately determined diminishing sources of variations. Accordingly, accuracy of bond strength measurement can grow preventing premature failure within the specimen and focusing on failure at the interface.

Finite element analysis is a powerful tool to predict strain and stress distributions within the specimen under the given loading and boundary conditions. There are methods to observe failure evolution during test in real time such as digital image correlation and acoustic emission measurement [5]. Finite element models are improved calibrating through acoustic emission measurements and digital image correlation. Subsequently,

finite element analysis can predict further, such as location of failure in the specimen whereas failure location is not detected by acoustic emission measurements [6].

1.2 LITERATURE REVIEW

There are many studies conducted on strength test applications in the literature. Dental research benefits bond strength test applications. Furthermore, diametral compression test constitutes an alternative approach to tensile strength and bond strength test applications. In recent years, it is also seen that diametral compression test is introduced to dental research.

1.2.1 Dentin-Adhesive Interface

The mechanism behind adhesion and the consequent interfaces between biomaterials and tissues is relatively complex [7]. Dentin-adhesive interface is an example of these complex systems where mechanical properties differ along this area of transition consisting of various material components and the mechanical properties of each material component taking part at the interface substantially contribute to adhesive's overall mechanical performance [8-10].

In addition to material components, complexity of the abovementioned mechanism also increases considering the factors involved in adhesion procedure. Enduring adhesion requires consideration of surface roughness and cleanliness, wettingand contact angle, providing sufficient flow of adhesive and paying attention on phase separation and solidification of adhesive [11].

Taking all the factors and parameters mentioned above into account, dentin-adhesive interface is the critical zone within the composite tooth restoration whose strength would determine whether the composite tooth restoration is able to survive under severe chemical and mechanical oral conditions conducting its service.

1.2.2 Dental Bonding Test Applications

The strength of dentin-adhesive interface is evaluated applying various bond strength tests. Bond strength test provides measurement of the distortion which will break the bond at the interface. There are various types of bond strength test such as shear bond strength, tensile bond strength, micro shear bond strength, micro tensile bond strength, push out and pull out [12-19].

Tensile bond strength test is conducted preparing a cylinder specimen where the normal of the interface plane matches direction of the tensile load applied. Shear bond strength test is conducted applying the load in a direction perpendicular to the normal of the interface plane. Micro shear and micro tensile bond strength tests emerge in order to measure bond strength of a small interface area (around 1 mm^2) [18-20]. Micro tests provide more accurate bond strength data eliminating cohesive failure of both composite and dentin where the interface area gets smaller comparing to macro tests [21].

The accuracy of bond strength data increases interpreting and eliminating the factors in strength test methods. As Armstrong expresses, the bond strength data depends on various factors such as presence of imperfection at the interface, geometry and size of sample and application of load [22]. In other words, applying pure tensile or shear load is

the challenge of bond strength tests where the stress distribution would be uniform within the specimen.

1.2.3 Diametral Compression Test

The nature of brittle materials does not provide the desired performance on direct tensile tests since these tests simply create stress concentrations where the sample is attached [23]. These stress concentrations result in premature failure of specimen in the grips [24]. The indirect tensile test or Brazilian test overcomes this problem and measures the tensile strength of brittle materials. The indirect tensile test was separately invented by Carneiro and Barcellos in Brazil and by Akazawa in Japan [25-27]. It is also called as diametral compression test or the split tensile test [28]. The Brazilian test has a wide variety of application areas where it measures tensile strength of rock [29], concrete [30], cohesive soils [28], pressed metal powder [31], pharmaceutical tablets [32], human enamel [24] and also bonding strength of concentric composites in dental research [5].

The procedure of indirect tensile test is relatively simple both in sample preparation and loading the sample since it does not require to fix the sample to any grips and the sample is conveniently loaded by placing it between two parallel load blocks [28].

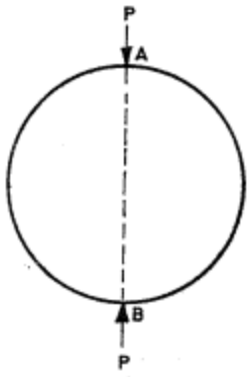

Figure 1.1: Test arrangement of split test [28].

As Ramanathan expresses, the test is conducted by positioning the disc sample across its diameter between two parallel load blocks which compress the sample (Figure 1.1) [28]. Particularly, Jonsen points out that the Brazilian test generates tensile stress which is perpendicular to the loading axis [31].

1.2.4 Diametral Compression Test in Dental Applications

Diametral compression test is applied to evaluate both tensile strength and bond strength. Bond strength data is obtained when the test is conducted on a dentin disc specimen filled with composite in the middle [5]. Tensile strength data is provided when the test is applied on a monolithic enamel disc specimen [24].

The results obtained from diametral compression test shows significant difference comparing to tensile test data from literature. According to the study Zaytsev conducted, tensile strength of enamel obtained from diametral compression test is 39.9 ± 4.7 MPa where tensile strength of enamel obtained from tensile test is 33-35 MPa [33].

The advantages of diametral compression bond strength test stated by Huang are that sample is prepared conveniently, sample does not prematurely fail, failure mode is more consistent and there is less variation in the obtained bond strength results [34].

1.3 SCOPE OF WORK

Success of dental restorations can be improved when reliable data is generated from bond strength tests and finite element analysis on dentin-adhesive interface. Diametral compression test is an alternative test method in order to obtain more accurate bond strength data where complexity of other test methods is eliminated. Moreover, it provides tensile and shear tests using the same test setup thanks to its generous design.

On the other hand, finite element analysis is a quite powerful tool in order to obtain more insights on mechanics problems. The recent finite element analysis studies conducted on dental diametral compression tests are based on linear elastic materials [5, 34-37]. However, classical elastic continuum mechanics constitutes limitation on analysis of performance of dental restorative materials [38].

Accordingly, this study presents the application of a granular micromechanics based user defined nonlinear material model [39] which is implemented into a finite element analysis software (Simulia/ABAQUS V 6.13-3, Dassault Systémes, RI, USA) to analyze the abovementioned diametral compression test as a two dimensional plain strain mechanics problem. The aim of this study is to show predicting capabilities of granular micromechanics based user defined nonlinear material model comparing the numerical results of this study with the experimental results where different concrete disc samples are tested varying in flaw size and flaw orientation they contain (1) and conducting finite

element analysis on dentin-adhesive diametral compression bond strength test in order to reveal more insights about application of the test (2).

CHAPTER 2

DIAMETRAL COMPRESSION TEST

2.1 TEST APPLICATION

Experimental procedure and results of diametral compression test on concrete disc samples are obtained through personal contacts (Zhou Yu, University of Science and Technology Beijing, China).

Diametral compression test is conducted on concrete disc specimens with diameter of 50 mm and thickness of 30 mm where the intact specimen contains no flaw and the flaw length, L is 8 mm and 24 mm for small and big flaw, respectively and the flaw width is 1.5 mm under the same loading conditions and at different flaw orientations. The flaw orientations are 0°, 15°, 30°, 45°, 60°, 75° and 90°.

Concrete samples are prepared mixing cement, fine sand and water with the ratio of 4:2:1. First, concrete is moulded as a cylinder for 24 hours and cylinder samples are maintained for 28 days after taking samples away from the mould. Afterwards, concrete cylinders are cut into pieces where concrete disc samples are prepared slicing the concrete cylinders.

Each disc specimen is placed in between load blocks where load blocks are in contact with the curved surfaces of disc specimen. The loading is applied with rate of ~0.4 MPa/sec via WEP-600 universal testing machine.

2.2 NUMERICAL ANALYSIS

Numerical analysis is carried out implementing the granular micromechanics based user defined nonlinear material model into the commercial finite element analysis software. The required geometry, boundary condition, loading and material property parameters are selected according to the experimental application.

2.2.1 Material Model

In the recent work of Poorsolhjouy, the user defined nonlinear material model is created based on granular micromechanics approach to establish constitutive equations for cementitious materials [39]. According to Poorsolhjouy's research, granular micromechanics is a method which introduces material's microstructure and mechanical properties in micro scale into continuum model where it is considered that representative volume element of material is considered as a set of grains and each grain is in contact with its adjacent grains through various mechanisms in grain scale. In the model, macroscopic dissipation potential and Helmholtz free energy density functions are expressed using the volume averages of matching functions from intergranular contacts. The model uses a Clausius-Duhem type inequality in order to represent proper constitutive relationships for intergranular contacts after deriving the inequality for interactions of grain-pairs. Furthermore, constitutive equations in micro scale are calibrated in order overall material behavior to correspond toexperimental behavior. Poorsolhjouy's study points out that material behavior in macro scale strongly depends on loading path resulting from nonlinear intergranular force laws and that each intergranular contact undergo unique loading history in different directions.

User-defined nonlinear material model parameters	Concrete
E_{no}^{T}	7 kN/m
R	12
G_w	2 kN/m
B_n	$7x10^{-7}$ m
B_{wo}	$1.32x10^{-6}$ m
α_1	10.5
α_2	7
α_3	0.0012
α_4	0.0265 MPa^{-1}

Table 2.1: Material parameters of concrete [39]

According to Poorsolhjouy's study, the listed material model parameters (Table 2.1) are selected for concrete where E^{T}_{n0} is grain scale normal stiffness in tension, R is ratio of compression to tension in terms of grain scale elastic stiffness, G_w is grain scale elastic stiffness in shear. Following parameters of the model are explained according to Figure 2.1 [39]. B_n is inter-granular displacement where normal inter-granular force reaches to peak in tensile inter-granular force-displacement curve, B_{w0} is inter-granular shear yield parameter in tension, α_1, α_2 and α_3 are model parameters of creating shear damage parameter with respect to normal displacement in micro scale and α_4 is stiffness growth parameter related to the increase in confinement.

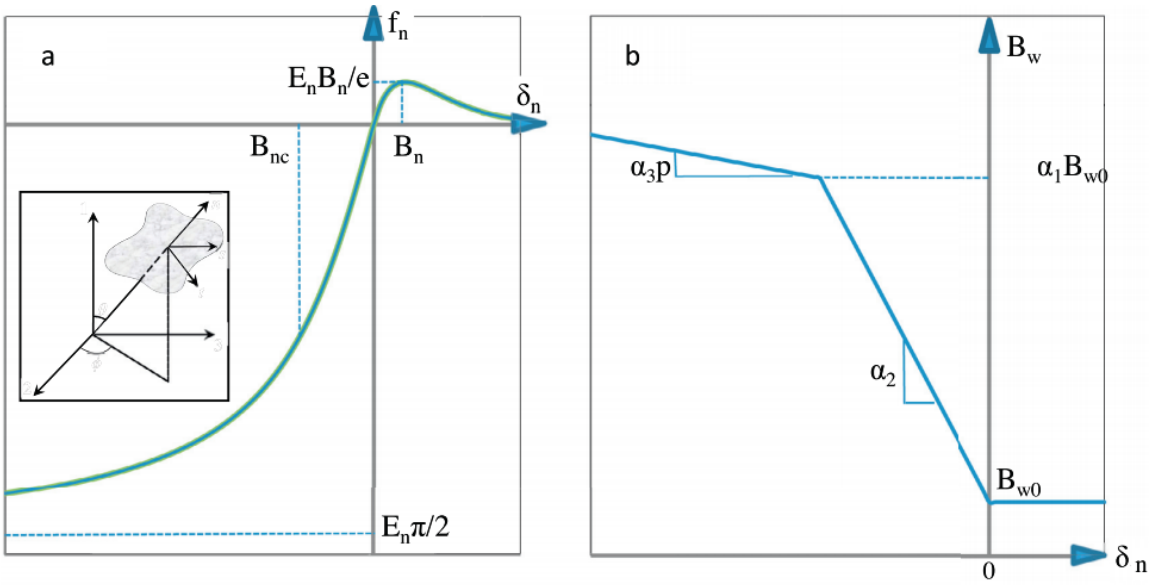

Figure 2.1: a – Intergranular normal force with respect to intergranular normal displacement where the inset presents the local coordinates, b – Shear damage parameter with respect to intergranular normal displacement [39]

2.2.2 Finite Element Model

In three dimensional finite element models, the Brazilian test is conducted on three different disc geometries. The first specimen contains no flaw. The second specimen contains flaw whose length is half of disc diameter. The third specimen also has flaw and its flaw length is one fourth of disc diameter. The loading is applied as displacement at two different loading rates. The first loading is applied as high loading rate where the total displacement of 1 mm is applied in 100 increments in y-direction. The second loading is applied as low loading rate where the total displacement of 0.2 mm is applied in 100 increments in y-direction. Different flaw orientations are created as 0°, 15°, 30°, 45°, 60°, 75° and 90° for models with small and big flaw keeping load fixed and rotating the disc around disc center. Figure 2.2 represents Brazilian test conducted on the disc containing big flaw where displacement load, U, is applied on top and bottom side surfaces of disc on y-axis as and arc of 5° from the disc center.

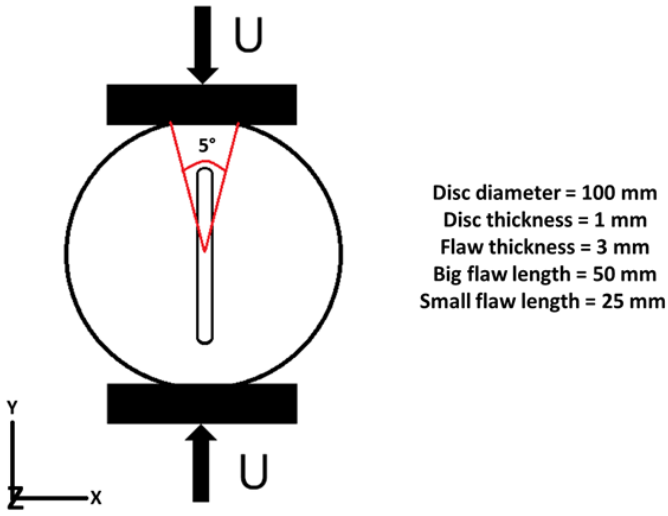

Figure 2.2: Representation of indirect tensile test considered in FE Model.

Figure 2.3 shows the boundary conditions and load applied in finite element model for the specimen having small flaw. In all models, the side line intersecting the center of load surface and lying on z-axis on both load surfaces are restricted in x-direction.

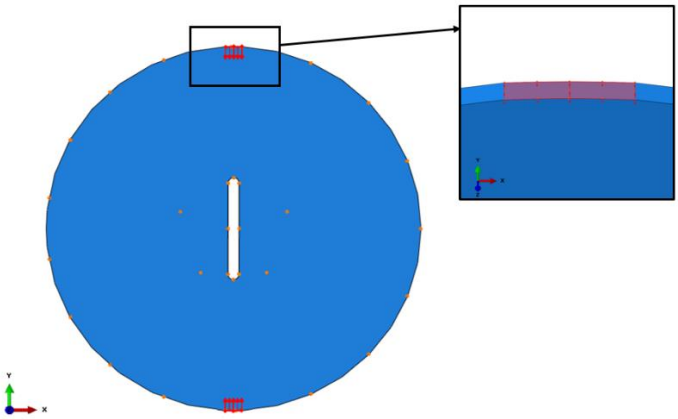

Figure 2.3: Displacement loading applied in FE model of disc with small flaw.

Moreover, displacement in z-direction is restricted for the whole disc where the case becomes a two dimensional plain strain mechanics problem.

Displacement load is applied on top and bottom side surfaces in y-direction at the abovementioned high and low loading rates as it is represented in Figure 2.3. Mesh is

generated using 4-node linear tetrahedral elements (C3D4). Figure 2.4 shows the meshed geometry of intact disc and discs with small flaw and big flaw at flaw orientation of 0°. Finally, the abovementioned user defined nonlinear material is assigned as material property of the whole disc which is concrete.

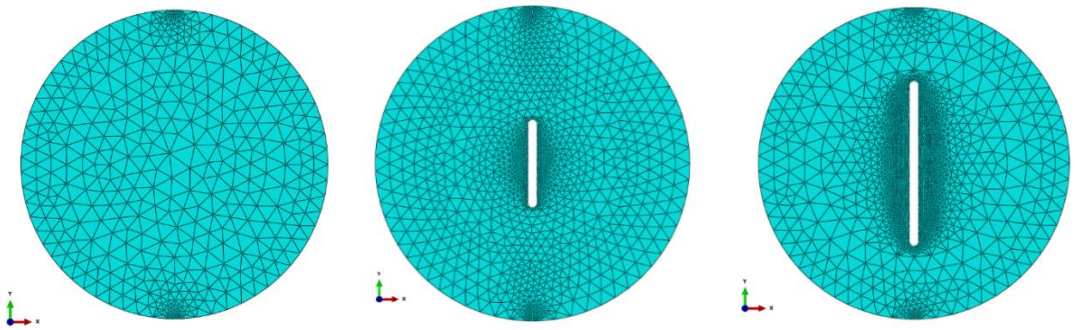

Figure 2.4: Meshed geometries of FE models. Intact disc vs. Disc with small flaw vs. big flaw

Particularly, loading is investigated in order to eliminate stress singularity and convergence issues experienced during finite element analysis. The contact between loading blocks and disc specimen is a line where stress becomes infinity. In this case, problem initially requires very small load application so that it can converge to a solution. Accordingly, this situation causes inability to conduct analysis with constant loading rate within the desired range of displacement loading since the initial load should be very small comparing to desired displacement loading. Therefore, two different finite element models are generated to measure the angle of arc load from disc center in order to eliminate line load issue and simulate a similar loading condition.

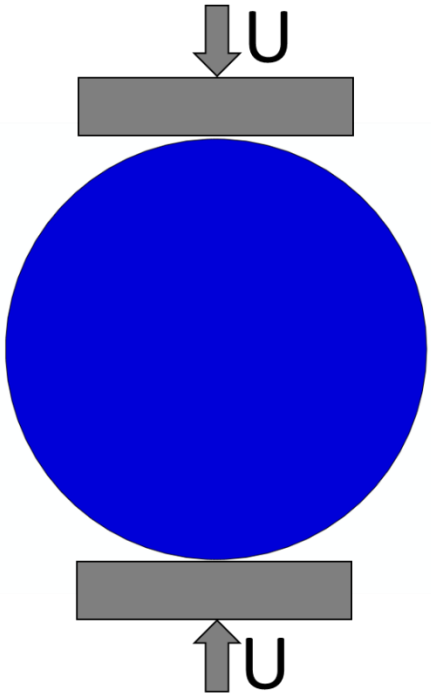

Figure 2.5: Finite element model of indirect tensile test where concrete specimen is compressed by two steel load blocks

One of the models is an intact concrete disc specimen whose 100 mm diameter and where the same meshing, boundary conditions and loading are applied as mentioned above in indirect tensile test. The other model is created assembling same concrete disc specimen with steel load blocks so that line load is provided on both sides (Figure 2.5).

The same meshing is applied on concrete disc specimen and this time, the side lines intersecting the center of upper load block's top surface and lower load block's bottom surface lying on z-axis are restricted in x-direction. Furthermore, displacement in z-direction is restricted in whole model. The line interaction between load blocks and disc specimen is assigned as hard contact and loading is applied uniformly on top surface of upper loading block in -y direction and on bottom surface of lower loading block in +y

direction as a total of 1 mm displacement loading with automatic time incrementation which allows to set initial load ~10^{-4} mm.

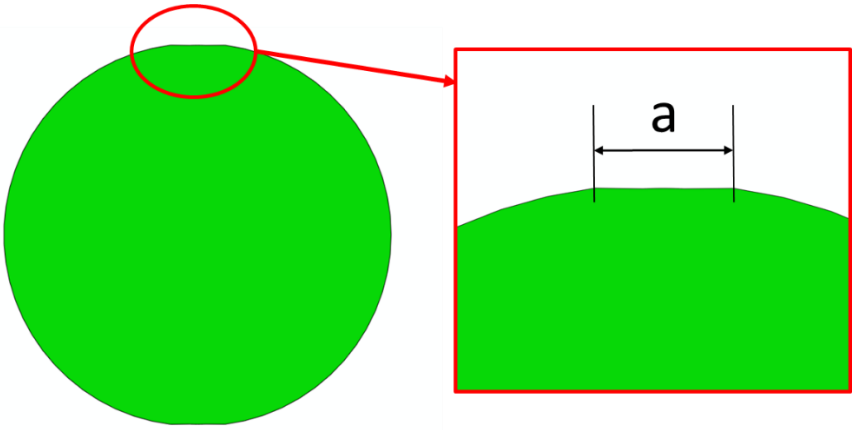

Figure 2.6: Contact surface flattening during indirect tensile test

The first model is analyzed using two different loading rates such as total displacement load of 1 mm in 100 increments and total displacement load of 0.2 mm in 100 increments.

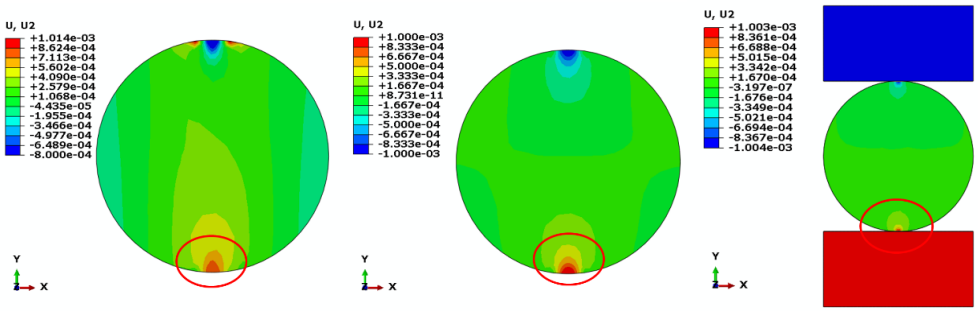

Figure 2.7: Displacement results in loading direction intact models with low and high loading rate and disc specimen between steel load blocks

The length of flattened side surface intersecting loading axis of all three models are compared to verify if application of load arc of 5° is the correct way to analyze the problem eliminating the line load and using constant loading rate (Figure 2.6).

According to Figure 2.7, length of flattened load surfaces, **a**, is calculated where the load surfaces of all models undergo same amount of displacement. The length, a, of intact models at both high and low loading rate is ~ 6 mm and the length, a, of concrete specimen between steel blocks is ~ 3.5 mm. This shows that conducting finite element analysis using load arcs of 5° and constant loading rate is reliable to simulate line load experienced in physical experiment.

Table 2.2 shows the range of calculation time, number of elements, number of nodes of all finite element analyses conducted on indirect tensile test on concrete specimens.

FE Model	CPU Time [sec]	Number of Elements	Number of Nodes
Intact disc	808.20-836.2	2740	959
Disc with small flaw	2622.1 - 3191.1	9806 - 10127	3151 - 3226
Disc with big flaw	7094.3 - 9066.6	29198 - 29267	7869 - 7882

Table 2.2: Calculation time, number of elements and nodes of FE Analyses.

2.3 RESULTS AND DISCUSSION

The data obtained from simulations are evaluated comparing the influence of flaw length, flaw orientation and loading rate in terms of both reaction forces and displacements on the load surfaces in the loading direction, RF_2 and U_2, respectively. Further, the contour plots are given for all cases in terms of octahedral normal strain and octahedral shear strain, which correspond to local volume change and local distortion, respectively, at the increment where each specimen reaches to failure. Failure is detected calculating the peak value of RF_2 for each case. Moreover, numerical results are compared with the experimental results of Yu's work where peak reaction forces from the numerical study are

converted to apparent tensile strength, σ using the equation, $\sigma=2F/\pi Dh$ setting F as peak reaction force, D as disc diameter and h as disc thickness. Besides, octahedral shear strain maps of all specimens at high loading rate are given next to the images of fractured specimens from the experimental study since the experimental study is conducted at one constant loading rate.

2.3.1 Yield Strength in Differet Flaw Orientations

As it is shown in Figure 2.8, the specimen having small flaw is stiffer than the specimen having big flaw when they both are at either high loading rate or low loading rate considering the specimen having small flaw has higher apparent tensile strength than the specimen having big flaw at all flaw orientations. Besides, both specimens with flaw are stiffer at high loading rate than at low loading rate considering that they have higher apparent tensile strength at high loading rate at all flaw orientations (Figure 2.8). These results are caused by the viscoelastic nature of granular materials where materials' response to loading is rate-dependent. In other words, the specimen becomes more elastic when the loading rate is high where the frequency of loading is high. On the other hand, specimen becomes softer when the frequency of loading is low that corresponds to low loading rate. Moreover, the apparent tensile strength slightly changes in the specimen having small flaw while flaw orientation angle is increasing at both loading rates, whereas the apparent tensile strength decreases between flaw orientations of 0° and 45° and then slightly changes up to 90° in the specimen having big flaw at both loading rates (Figure 2.8).

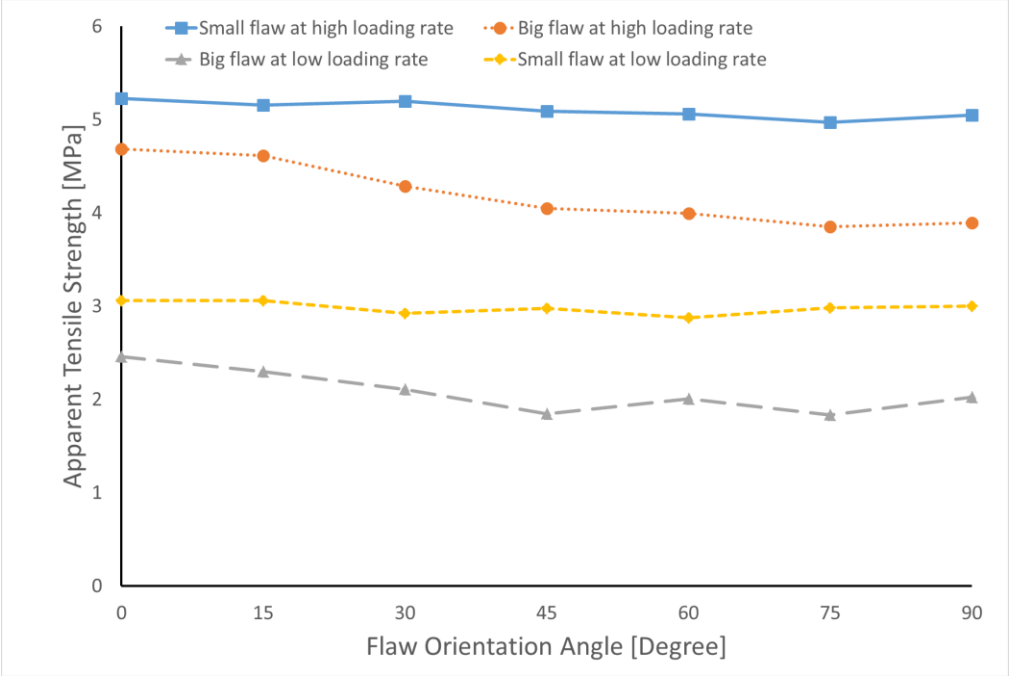

Figure 2.8: Apparent Tensile strength of both specimens with flaw at different flaw orientation and loading rates

The specimen with small flaw has the highest apparent tensile strength which are 5.23 MPa at flaw orientation of 0° at high loading rate and 3.06 MPa at flaw orientation of both 0° and 15° at low loading rate, whereas the specimen with big flaw has the highest apparent tensile strength which are 4.69 MPa at flaw orientation of 0° at high loading rate and 2.46 MPa at flaw orientation of 0° at low loading rate. Furthermore, the specimen with small flaw has the lowest apparent tensile strength which are 4.97 MPa at flaw orientation of 75° at high loading rate and 2.87 MPa at flaw orientation of 60° at low loading rate, whereas the specimen with big flaw has the lowest apparent tensile strength which are 3.85 MPa at flaw orientation of 75° at high loading rate and 1.83 MPa at flaw orientation of 75° at low loading rate.

2.3.2 Yield Strength vs. Displacement

Figure 2.9 and Figure 2.10 show that the specimen having small flaw has approximately the same pattern in terms of RF_2 with respect to U_2 at all flaw orientations at both loading rates while it is reaching to failure and the peak values of RF_2 are very close to each other at different flaw orientations.

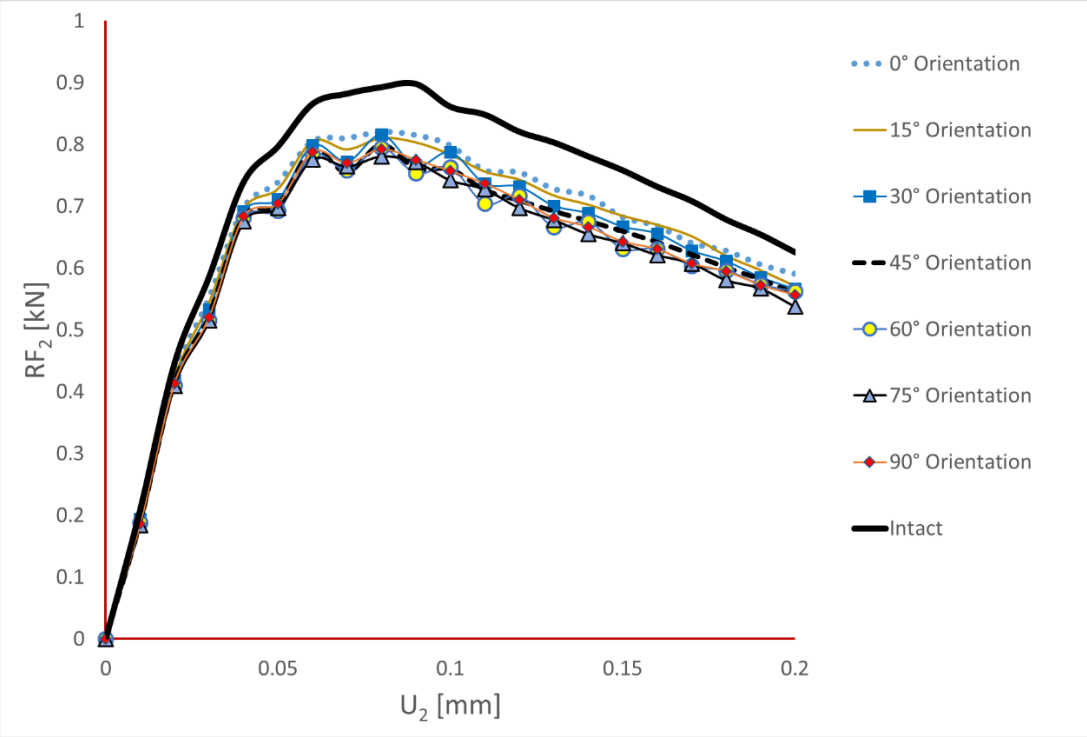

Figure 2.9: Reaction forces vs. displacement in loading direction (Small flaw at high loading rate)

Moreover, all intact specimen and the specimens with flaw undergo sudden decrease in RF_2 at low loading rate after failure whereas they do not undergo sudden decrease in RF_2 at high loading rate after failure at all flaw orientations (Figure 2.9, Figure 2.10, Figure 2.11 and Figure 2.12).

Figure 2.11 and Figure 2.12 show that the specimen having big flaw has approximately the same pattern in terms of RF_2 with respect to U_2 up to failure at different flaw orientations at both loading rates but the peak values of RF_2 are significantly different than each other.

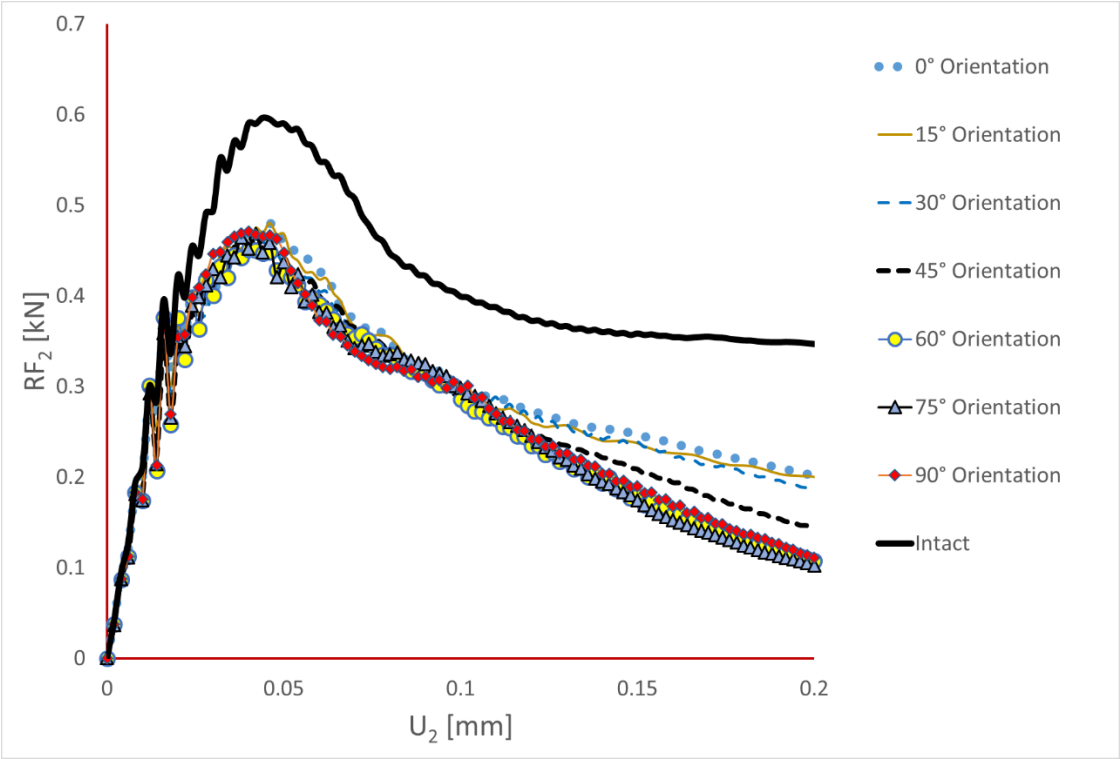

Figure 2.10: Reaction forces vs. displacement in loading direction (Small flaw at low loading rate)

The intact specimen is also stiffer at high loading rate than at low loading rate comparing peak values of RF_2 of intact specimen in Figure 2.9 and Figure 2.10. Likewise, Figure 2.9, Figure 2.10, Figure 2.11 and Figure 2.12 show that both specimens with flaw have lower strength than the intact specimen at both loading rates considering that the peak value of RF_2 designates failure. These results are expected since flaw can be considered as weakness within disc specimen and creating a flaw or increasing flaw size would cause a weaker specimen whose apparent tensile strength would be lower.

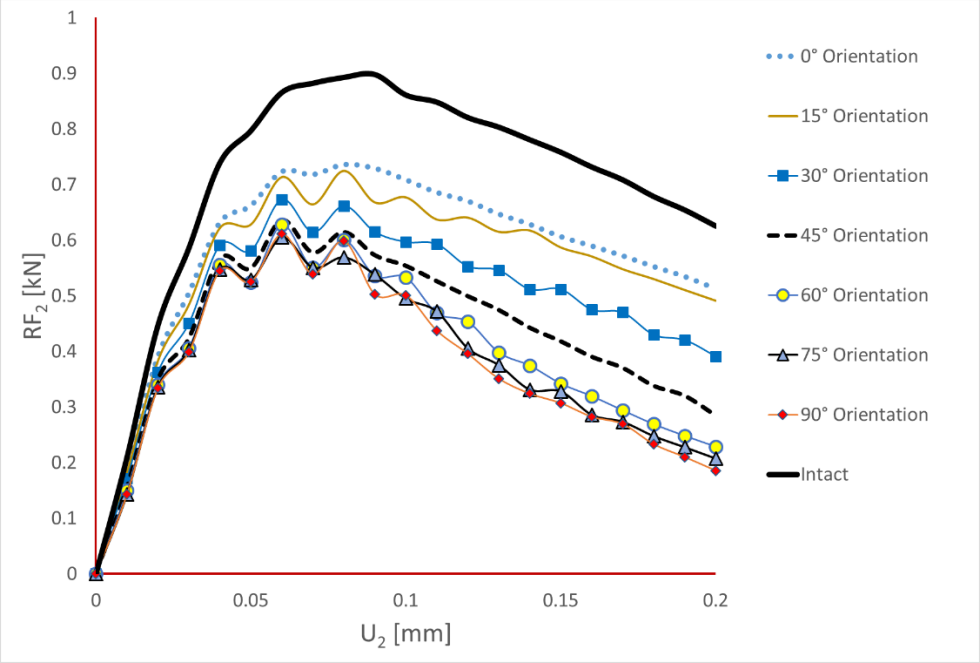

Figure 2.11: Reaction forces vs. displacement in loading direction (Big flaw at high loading rate)

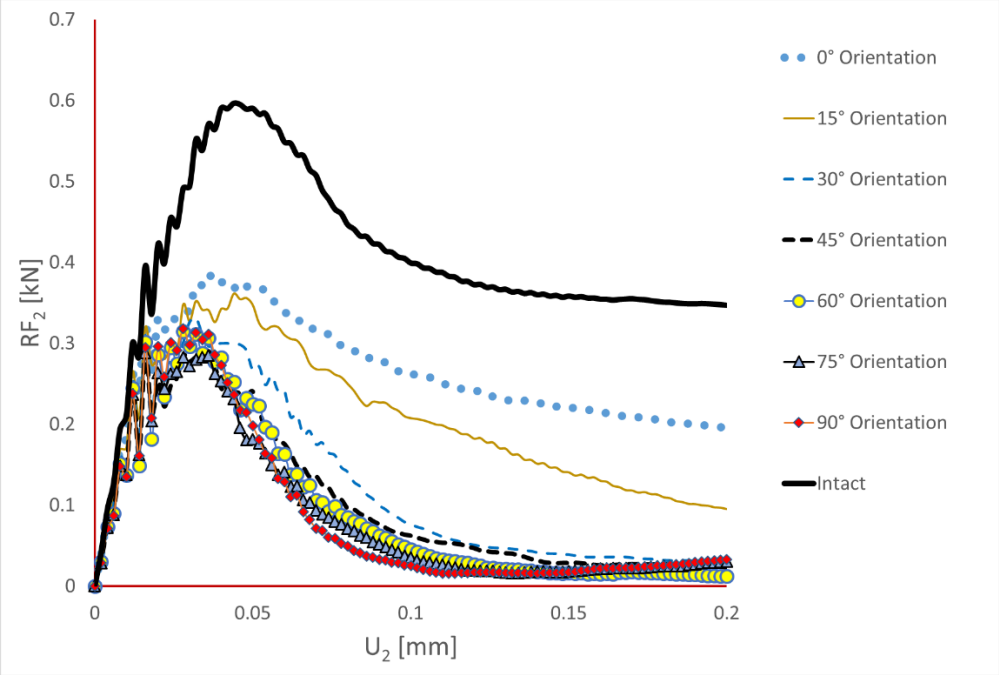

Figure 2.12: Reaction forces vs. displacement in loading direction (Big flaw at low loading rate)

2.3.3 Octahedral Normal Strain Maps

Figure 2.13 shows the octahedral normal strain maps in xy-plane at all flaw orientations for all specimens using the same scale for strain magnitude where each specimen reaches to its peak value of RF_2. The results at high loading rate are presented on the left side whereas the results at low loading rate are presented on the right side. Mainly, the vicinity of load surfaces undergoes significant shrinkage in all cases and the shrinkage area is bigger at high loading rate than at low loading rate. The area under the load surfaces of intact specimen is under shrinkage at both loading rates where local volume change is bigger at high loading rate. Both specimens having big and small flaw undergo significant shrinkage around flaw tips and flaw center and load surfaces at flaw orientations between 0° and 30° at high loading rate whereas they undergo significant shrinkage only around flaw tips and load surfaces at flaw orientations between 45° and 90° at high loading rate. Besides, significant dilation is observed at the flaw tips in the specimen with big flaw at flaw orientations between 0° and 45° at both loading rates whereas significant dilation is observed at the flaw tips in the specimen with small flaw at flaw orientations between 0° and 75° at both loading rates and between flaw tips and flaw center at flaw orientation of 90° at low loading rate. The area under load surface and the vicinity of flaw tips are under significant shrinkage when the specimen with big flaw is at flaw orientations between 15° and 90° and the specimen with small flaw is at flaw orientations between 30° and 90° at low loading rate whereas only vicinity of load surface undergoes significant shrinkage when the specimen with big flaw at flaw orientation of 0° and the specimen with small flaw at flaw orientations of 0° and 15° at low loading rate.

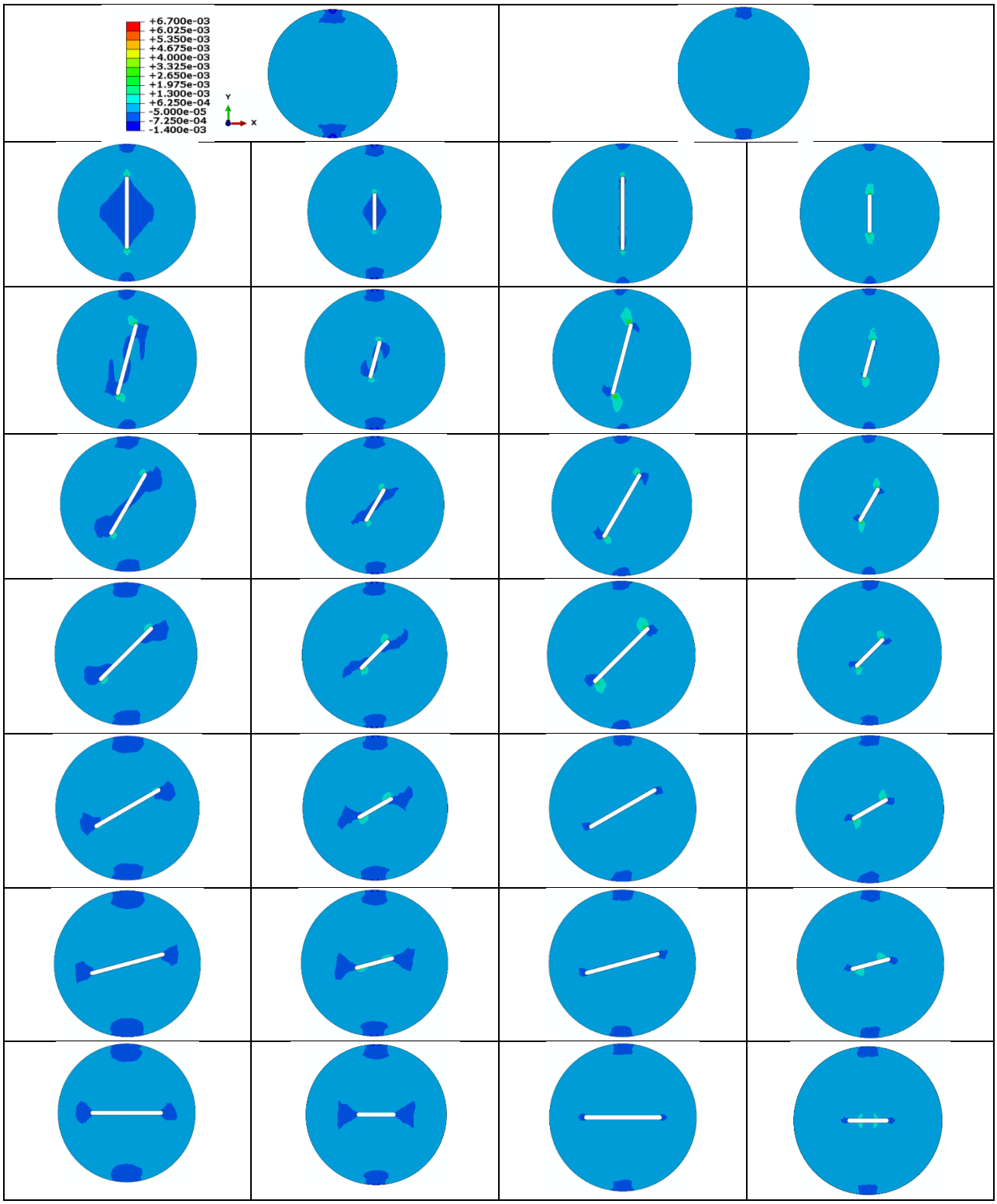

Figure 2.13: Octahedral normal strain maps in intact specimen, specimens with big and small flaw at high loading rate and at low loading rate

2.3.4 Octahedral Shear Strain Maps

Figure 2.14 shows the octahedral shear strain maps in xy-plane at all flaw orientations for all cases using the same scale for strain magnitude where each specimen reaches to its peak value of RF_2. The results at high loading rate are presented on the left side are compared with the results at low loading rate on the right side. Local distortion is significantly higher in vicinity of load surface in intact specimen at both loading rates where the area distorted at high loading rate is higher than at low loading rate. The significantly distorted area is between flaw tips and load surface along the loading axis in both specimens having flaw when they both are at flaw orientation of 0° at both loading rates whereas the significantly distorted area is between flaw tips and load surface in both specimens having flaw when they both are at flaw orientation of 15° and at both loading rates. The significant local distortion is observed only at the flaw tips in the specimen with big flaw at flaw orientations between 30° and 60° at high loading rate and at flaw orientations of 30° and 45° whereas the significant distortion is observed between flaw tips and flaw center at flaw orientation of 75° at high loading rate. Furthermore, significant local distortion is seen in vicinity of flaw tips and load surfaces in the specimen with small flaw at flaw orientations of 45° and 60° at high loading rate whereas local distortion is significant only at the flaw tips at flaw orientations of 45° and 60° at low loading rate. Local distortion is observed to be significant between flaw tip and load surface in the specimen with small flaw at flaw orientation of 30° at both loading rates. The area between flaw tips and flaw center and vicinity of load surface are under significant distortion in the specimen with small flaw at flaw orientation of 75° at high loading rate while only the area between flaw tips and flaw center is under significant distortion at flaw orientation of 75°

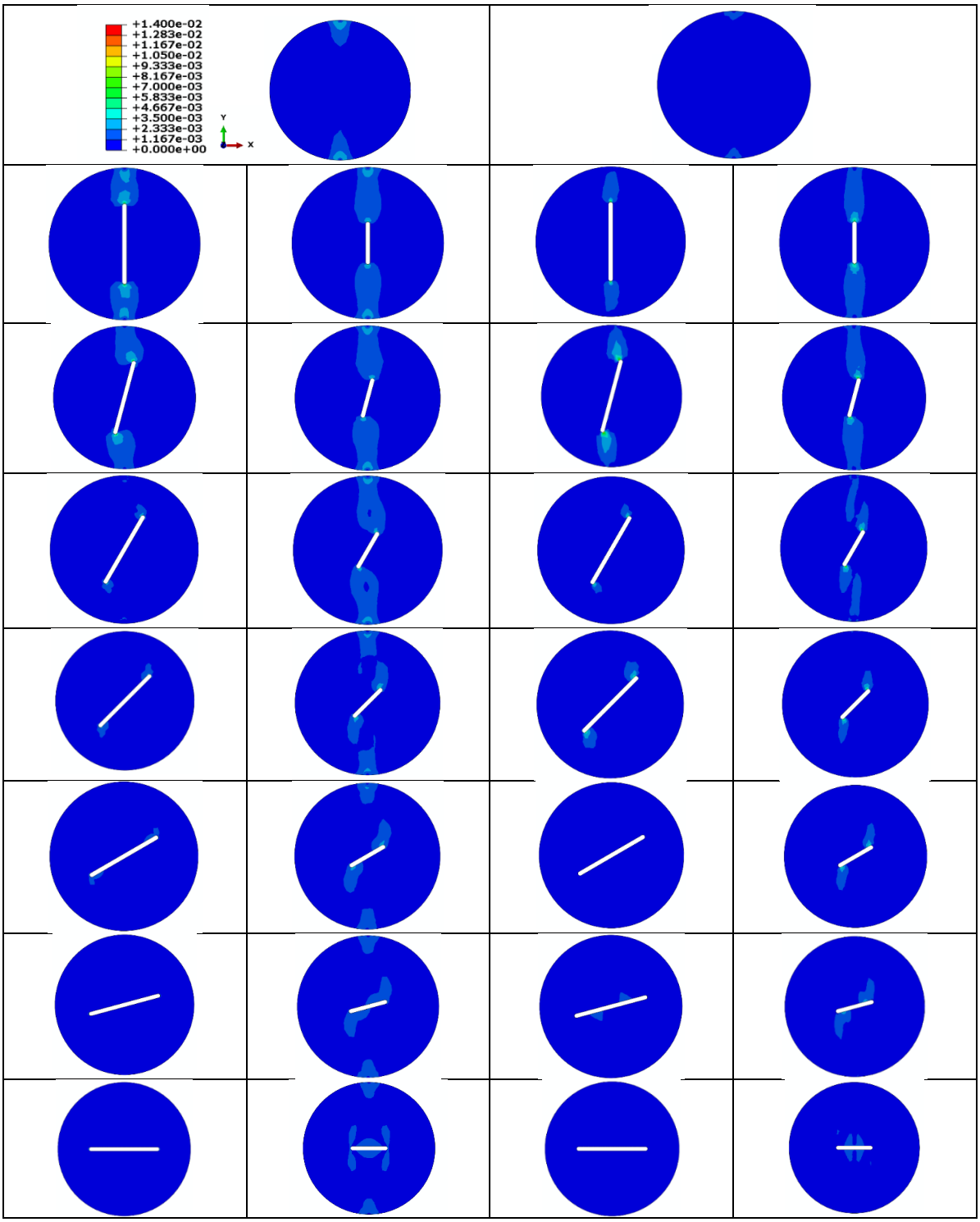

Figure 2.14: Octahedral shear strain maps in intact specimen, specimens with big and small flaw at high loading rate and at low loading rate

at low loading rate. Moreover, it is observed that the specimen with small flaw undergoes significant local distortion around flaw tips, in center of flaw and under load surface at flaw

orientation of 90° at high loading rate while significant local distortion is observed only in the area between flaw tips and center of flaw in the same specimen at the same flaw orientation at low loading rate.

2.3.5 Diametral Expansion vs. Displacement

Diametral expansion reveals how the specimen behaves in terms of expansion along its diametral axis (x-axis) during loading. The displacement values along x-axis, U_1 of points which are at the intersection of diametral axis with specimen edges are obtained (Figure 2.15) and plotted with respect to displacement loading, U_2.

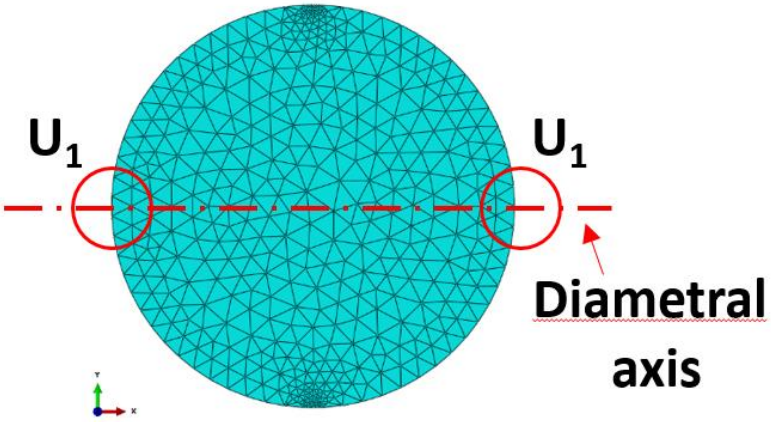

Figure 2.15: The points whose displacements along x-axis are obtained to show diametral expansion.

Diametral expansion results of both specimens with small and big flaw are plotted at all flaw orientations with results of intact specimen at both high and low loading rates. Generally, the pattern of all results reveals nonlinearity of the mechanics problem looking at how nonlinearly the displacement along x-axis of edge points increases with respect to loading displacement (Figure 2.16, Figure 2.17, Figure 2.18 and Figure 2.19).

It is also seen that introducing flaw within the disc increases diametral expansion comparing to the results with respect to intact specimen at both loading rates (Figure 2.16, Figure 2.17, Figure 2.18 and Figure 2.19). Additionally, the lowest diametral expansion is experienced among the specimens with flaw when the flaw angle is 0°.

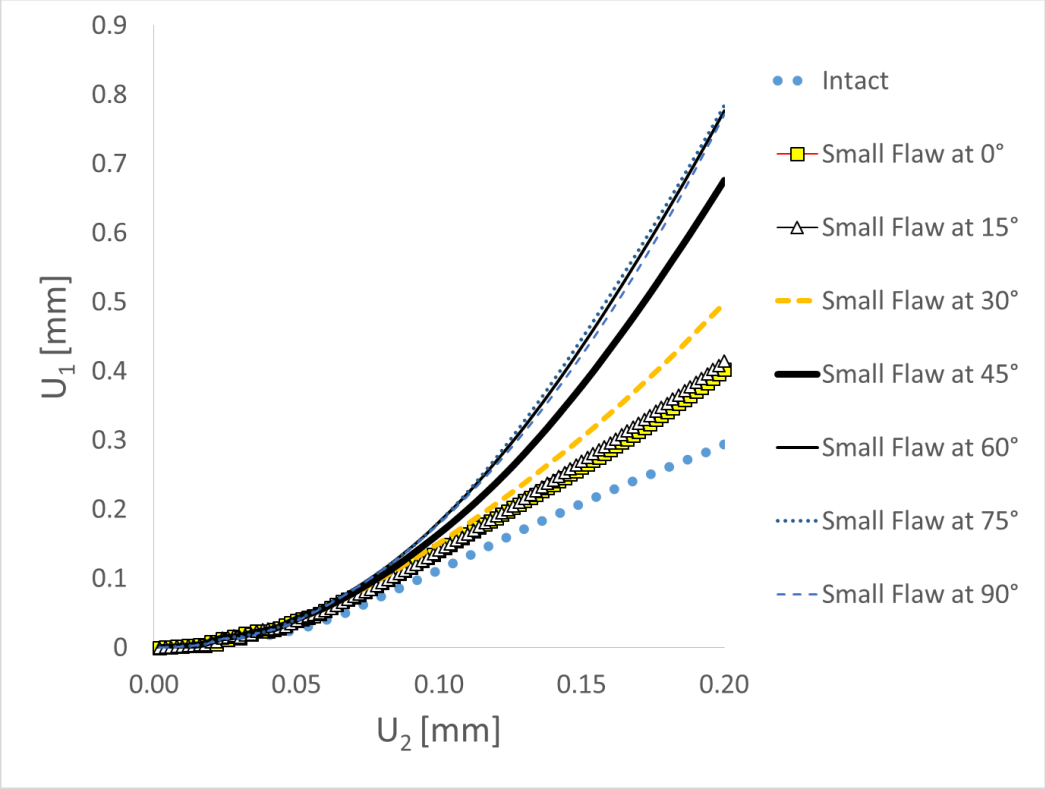

Figure 2.16: Diametral expansion results of intact specimen and specimen with small flaw at low loading rate.

Figure 2.18 shows that diametral expansion increases increasing the flaw orientation angle when the specimen is with big flaw and at high loading rate.

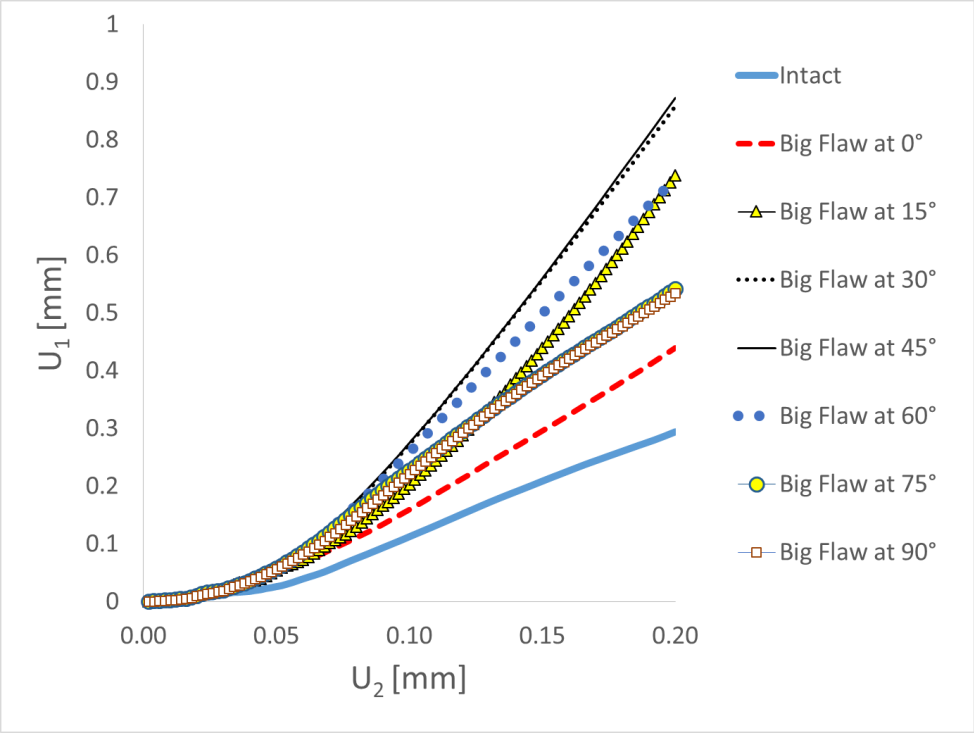

Figure 2.17: Diametral expansion results of intact specimen and specimen with big flaw at low loading rate.

As it is seen in Figure 2.16, diametral expansion increases increasing flaw orientation angle but maximum diametral expansion is reached at flaw orientation of 60° and it is almost the same at flaw orientations of 75° and 90° when the specimen is with small flaw and at low loading rate. The highest diametral expansion is seen at flaw orientations of 30° and 45° when the specimen with big flaw is at low loading rate (Figure 2.17). On the other hand, maximum diametral expansion is observed when the small flaw having specimen is at flaw orientation of 75° (Figure 2.19).

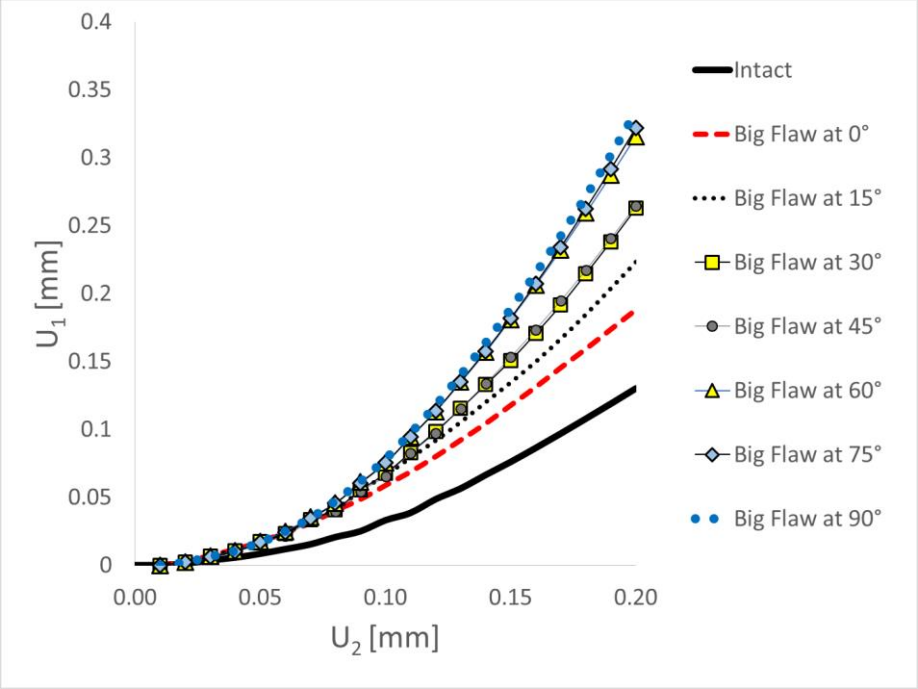

Figure 2.18: Diametral expansion results of intact specimen and specimen with big flaw at high loading rate.

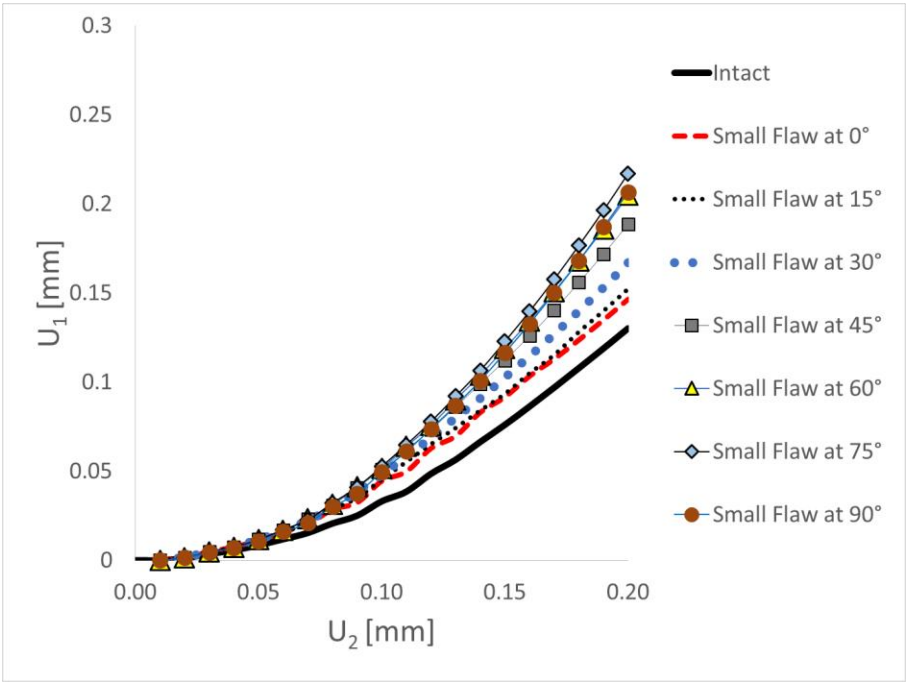

Figure 2.19: Diametral expansion results of intact specimen and specimen with small flaw at high loading rate.

2.3.6 Comparison with Experimental Results

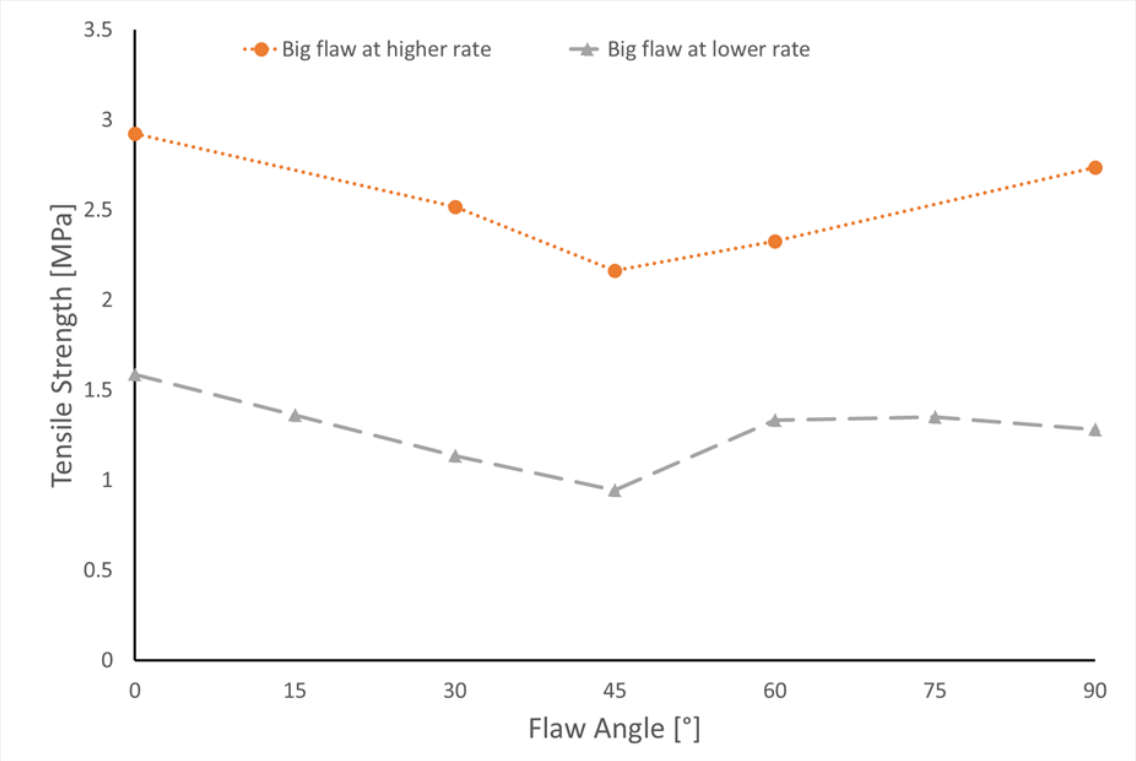

Figure 2.20: Tensile strength results of specimens with flaw in experimental study

Figure 2.20 shows the experimental results of indirect tensile test conducted on concrete disc specimens. These experimental results are compared with results of numerical study. The specimen with small flaw is stiffer than the specimen with big flaw at all flaw orientations considering the specimen with small flaw has higher tensile strength than the specimen with big flaw at all flaw orientations as it is predicted by the results of numerical study (Figure 2.8). Moreover, it is seen that apparent tensile strength in both specimens with flaw slightly change at flaw angles of 0° and 90° comparing strength values at low and high loading rate in Figure 2.8 and tensile strength values in Figure 2.20. Furthermore, strength of the specimen with big flaw constantly decreases between flaw orientations of 0° and 45°, and slightly changes between flaw orientations of 60° and 90°

around the tensile strength value at flaw orientation of 0° both in Figure 2.20 and at high and low loading rates in Figure 2.8.

Figure 2.21 shows the octahedral shear strain maps in xy-plane at all flaw orientations for all specimens using the scales for strain magnitude which are fixed at the values of octahedral shear strain at failure of each specimen and where contour plots present the octahedral shear strain maps of each specimen beyond its failure at high loading rate. Moreover, each case is compared with fracture images of corresponding specimen from experimental study on its left side where the experimental study is conducted at single loading rate and the results of the specimen having small flaw are missing at flaw orientation of 15° and 75°. Mainly, it is seen that the areas of high octahedral shear strain concentrations (grey colored) match the fracture pattern in the experimental results for each case compared. In detail, numerical study shows that intact specimen is heavily distorted along the loading direction after failure where the experimental image shows that the intact specimen is fractured along the loading direction. Both specimens with big and small flaw are heavily distorted between load surface and flaw tips along the loading direction at flaw orientation of 0° whereas the corresponding experimental images show that both specimen are fractured along loading direction. Further, both specimens undergo high local distortion between load surface and flaw tips at flaw orientation of 15° in numerical study where the experimental study only shows the specimen with big flaw fractured between flaw tips and load surface at the same flaw orientation. The fracture images of specimen with big flaw show two separate cracks at flaw orientations between 30° and 60°. One of these separate cracks is between flaw tip and load surface and the other one is at the edge along the longitudinal flaw axis.

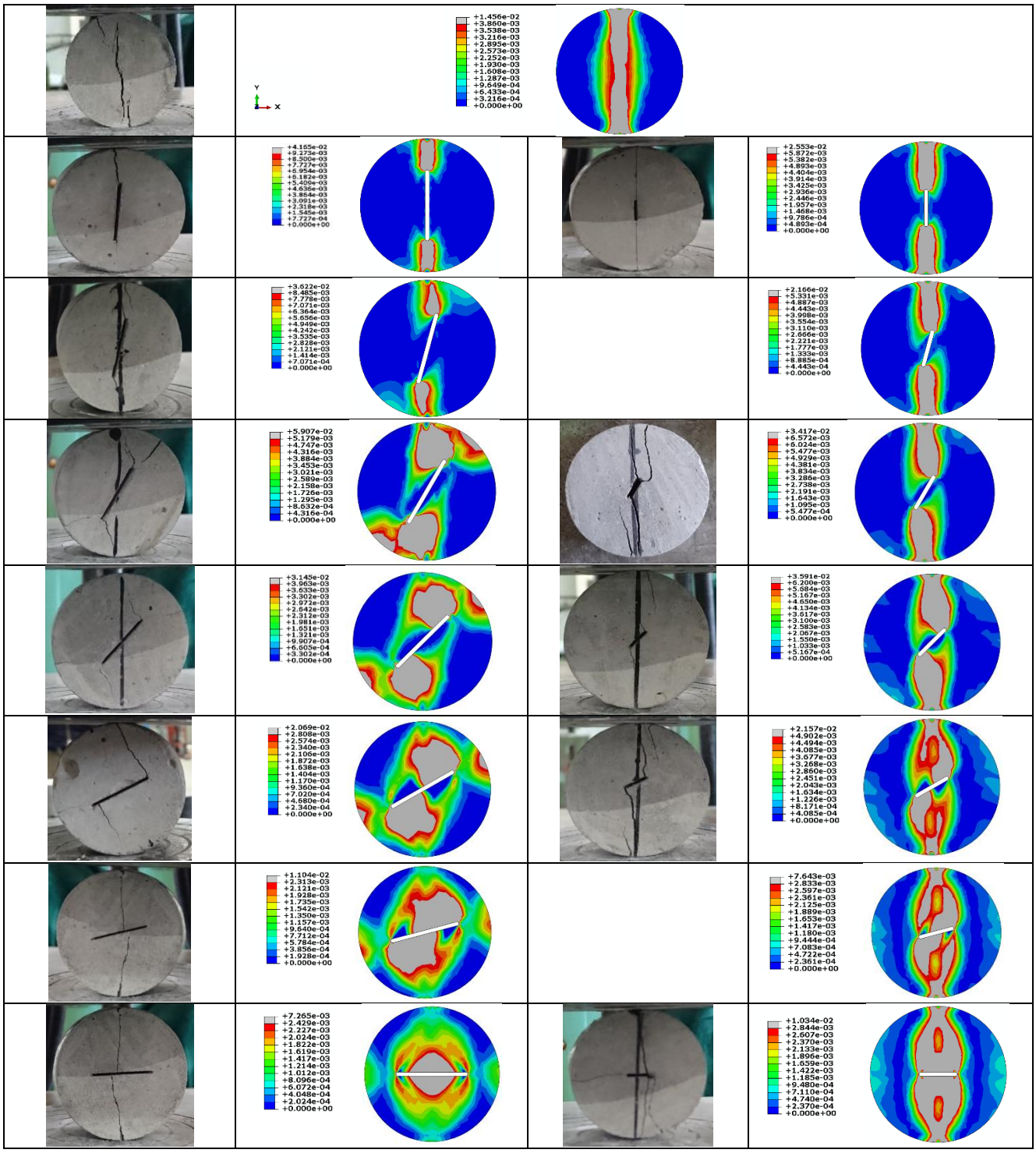

Figure 2.21: Experimental fracture patterns vs. octahedral shear strain maps of intact specimen and specimens with big and small flaw at high loading rate

Octahedral shear strain maps of the same cases from this numerical study show that the area between flaw tip and load surface and the area at the edge on the longitudinal flaw axis are highly distorted. It is also observed in images from the experiment that fracture is on the loading axis passing through the vicinity of center of flaw when the specimen with big flaw is at flaw orientations at 75° and 90° whereas octahedral strain maps show that the specimen with big flaw is highly distorted in the area between flaw tips and flaw center at flaw orientation of 75° and around flaw center at flaw orientation of 90°. Moreover, fracture is between load surface and flaw tips in the specimen with small flaw at flaw orientations between 30°, 45°, 60° and 90° in experimental results whereas numerical results show that the specimen with small flaw is highly distorted in the area between flaw tips and load surfaces at flaw orientations between 30° and 60° and in vicinity of flaw along the loading axis at flaw orientations of 75° and 90°.

CHAPTER 3

DIAMETRAL COMPRESSION TEST ON DENTIN-ADHESIVE INTERFACE

3.1 FINITE ELEMENT MODELS OF DENTIN-ADHESIVE INTERFACE

In this chapter, finite element analysis is conducted creating various three dimensional finite element models in order to simulate the application of diametral compression test as bond strength test. Three different geometries are created to represent dentin-adhesive interface which are intact, concentric and sandwich models. Additionally, ring model is created in order to reveal post-debonding mechanism. Both geometries are used in order to generate various models assigning different material properties.

The material properties are given considering that the materials creating dentin-adhesive interface vary as dentin-like, composite-like, polymer and steel. Table 3.1 shows the given material properties of each material in terms of the parameters of material model and linear elastic materials.

User-defined nonlinear material parameters	Dentin-like material	Composite-like material
E_{no}^{T}	7 kN/m	4 kN/m
R	12	12
G_w	2 kN/m	2 kN/m
B_n	$7x10^{-7}$ m	$7x10^{-7}$ m
B_{wo}	$1.32x10^{-6}$ m	$1.32x10^{-6}$ m
α_1	10.5	10.5
α_2	7	7
α_3	0.0012	0.0012
α_4	0.0265 MPa^{-1}	0.0265 MPa^{-1}

Linear material parameters	Steel Post	Polymer
Young's Modulus	203 GPa	4 GPa
Poisson's ratio	0.3	0.3

Table 3.1: Material parameters assigned in concentric FE models

In all models generated, identical loading is applied which is total displacement of 0.05 mm in 100 increments in y-direction.

Intact models are created using abovementioned boundary conditions and displacement loading in indirect tensile test on concrete intact disc specimen. This time, the diameter of intact disc model is 5 mm and the thickness is 2mm, material is assigned as dentin-like in one intact model and the other intact model is composite-like material. Furthermore, mesh is generated using 4-node linear tetrahedral elements (C3D4) in intact models.

3.1.1 Concentric Model

The concentric model is generated considering the cases with perfect, weak, soft and stiff interface. Monolithic disc geometry is partitioned into two different sections where it is considered that two different sections are perfectly bonded. These two sections are inner layer and outer layer where the outer diameter of outer layer is 5 mm and the diameter of inner layer is one third of the diameter of the outer layer. Figure 3.1 represents the concentric model where the outer layer is assigned as dentin-like material and inner layer is assigned as adhesive.

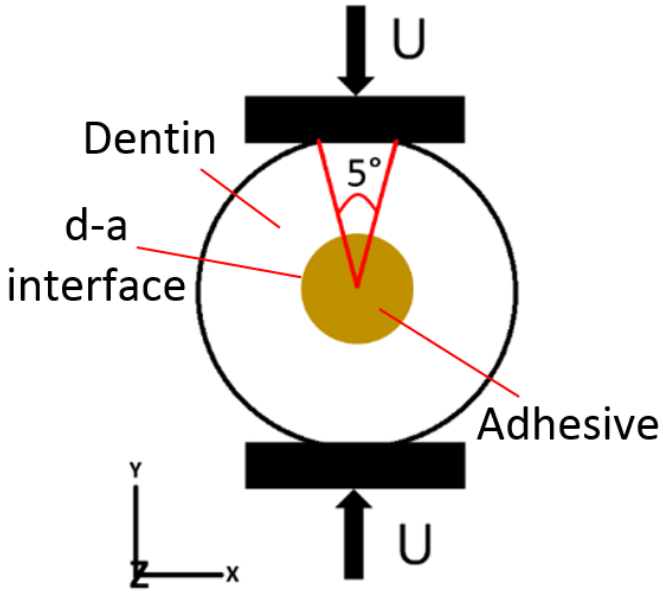

Figure 3.1: Representation of concentric model with dentin and adhesive.

Displacement load, U, is applied on top and bottom side surfaces of disc on y-axis as and arc of 5° from the disc center. In all models, the side line intersecting the center of load surface and lying on z-axis on both load surfaces are restricted in x-direction. Moreover, displacement in z-direction is restricted for the whole disc where the case becomes a two dimensional plain strain mechanics problem.

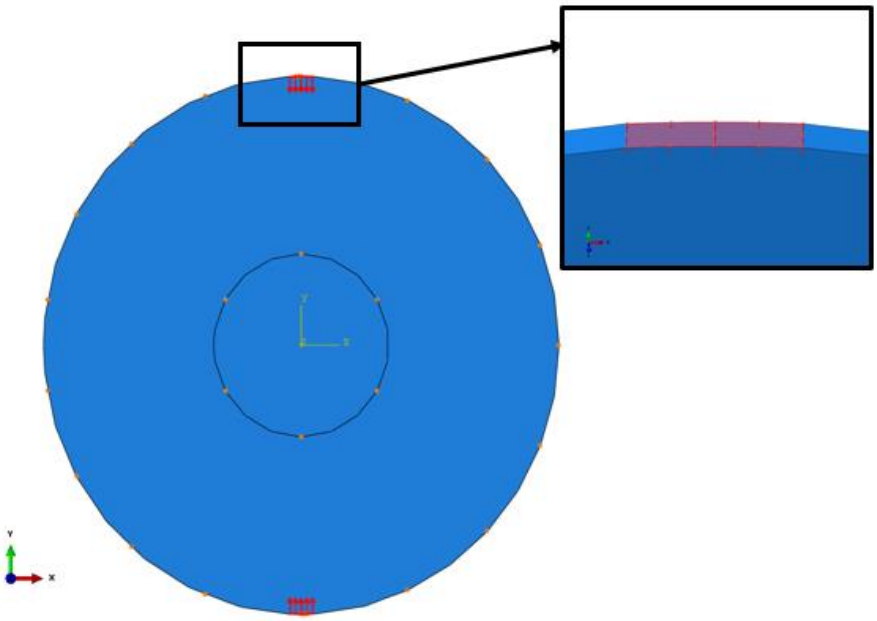

Figure 3.2: Displacement loading applied in concentric model.

Displacement load is applied on top and bottom side surfaces in y- it is represented in Figure 3.2. Mesh is generated using 4-node linear tetrahedral elements (C3D4). Figure 3.3 shows the meshed geometry of concentric model.

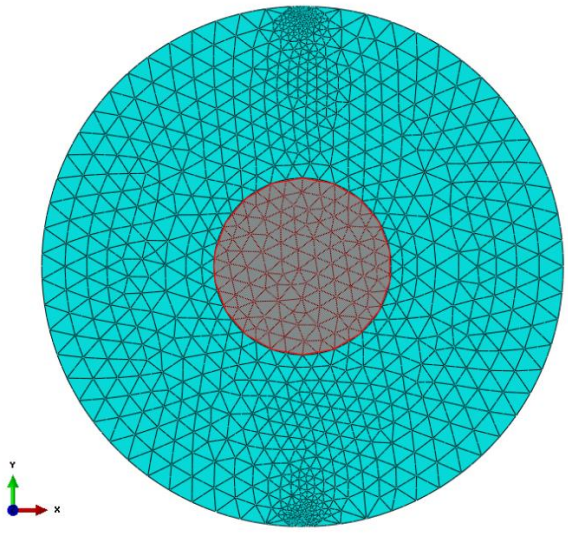

Figure 3.3: Meshed geometry of concentric model.

	Weak Interface	Soft Interface	Stiff Interface
Normal linear interface coefficient (k_n)	0	0.07	7
Shear linear interface coefficients ($k_s = k_t$)	0	0.035	3.5

Table 3.2: Linear interface coefficients assigned in FE analyses

Additionally, the concentric model with imperfect interface is created generating geometries of outer layer and inner layer separately and assembling them. Linear interface coefficients are assigned as contact properties at the interface to represent weak, soft and stiff interface (Table 3.2).

Interface Property	Outer Layer Material	Inner Layer Material
Perfect	Composite-like	Dentin-like
Perfect	Dentin-like	Composite-like
Perfect	Composite-like	Steel Post
Perfect	Dentin-like	Steel Post
Perfect	Dentin-like	Polymer
Stiff	Dentin-like	Polymer
Soft	Dentin-like	Polymer
Weak	Dentin-like	Polymer

Table 3.3: List of concentric models with interface property and materials selection

Meshing, boundary conditions and loading are applied the same as the abovementioned concentric model with perfect interface. Finally, related material

properties are assigned to each model. The concentric models generated are listed in Table 3.3.

3.1.2 Ring Model

The ring model is created taking post-debonding at the interface into account. A circular hole is introduced into the center of the disc in order to create the disc specimen. Outer diameter of ring geometry is the same as the concentric model which is 5 mm and inner diameter is one third of the outer diameter. Figure 3.4 represents the ring model where the material is assigned as dentin-like material.

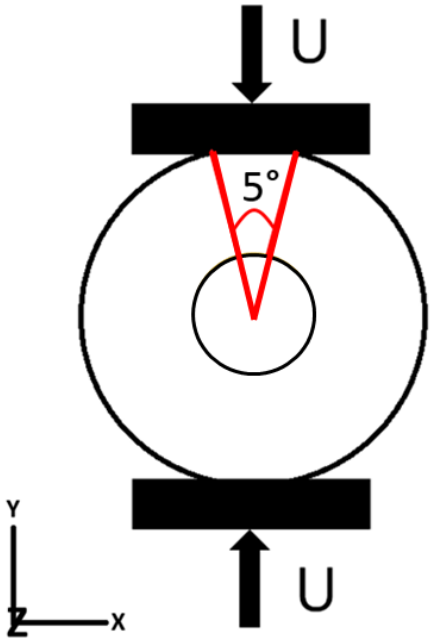

Figure 3.4: Representation of dentin ring model.

Boundary conditions and loading is applied same as concentric model. Figure 3.5 presents loading applied on side surfaces along y direction. Mesh is generated using 4-node linear tetrahedral elements (C3D4). Figure 3.6 shows the meshed geometry of ring model.

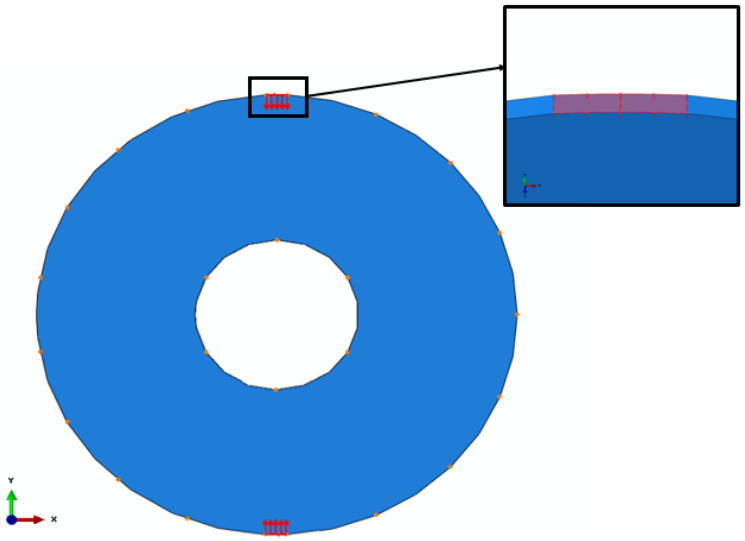

Figure 3.5: Displacement loading applied in ring model.

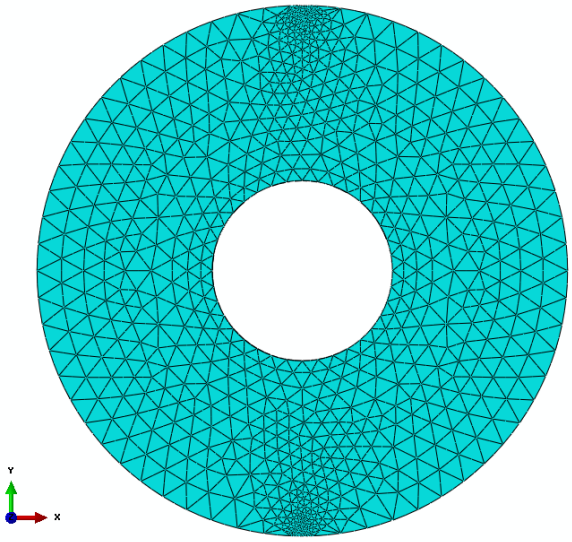

Figure 3.6: Meshed geometry of ring model.

3.1.3 Sandwich Model at Different Interface Orientations

The sandwich model is generated using monolithic disc geometry whose diameter is 5 mm. Monolithic disc geometry is partitioned into halves which are two different sections. It is considered that these two different sections are perfectly bonded. Figure 3.7 represents the sandwich model where the left layer is assigned as composite-like material and right layer is assigned as dentin-like material and the interface orientation, θ, is 0°.

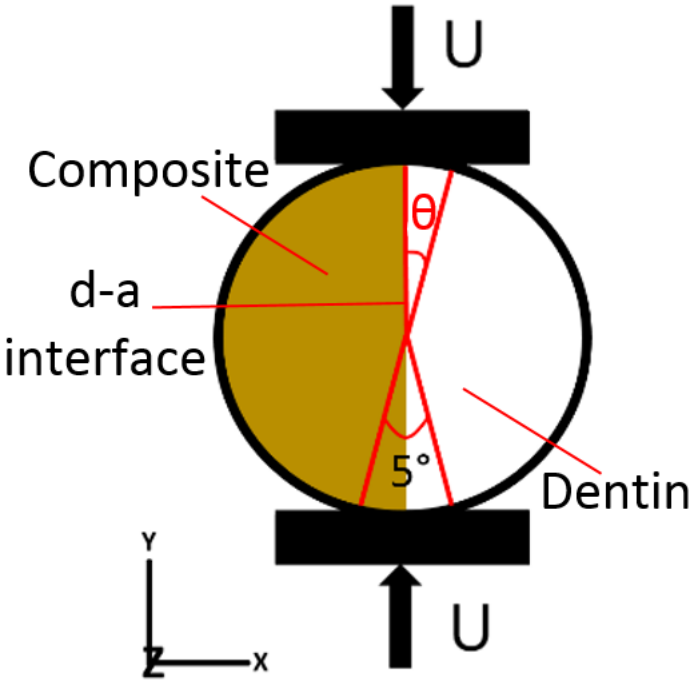

Figure 3.7: Representation of sandwich model with dentin and composite at interface orientation of 0°.

Displacement load, U, is applied on top and bottom side surfaces of disc on y-axis as and arc of 5° from the disc center. In all models, the side line intersecting the center of load surface and lying on z-axis on both load surfaces are restricted in x-direction. Moreover, displacement in z-direction is restricted in the whole disc in order to make the

case become a two dimensional plain strain mechanics problem. Displacement load is applied on top and bottom side surfaces in y- it is represented in Figure 3.8.

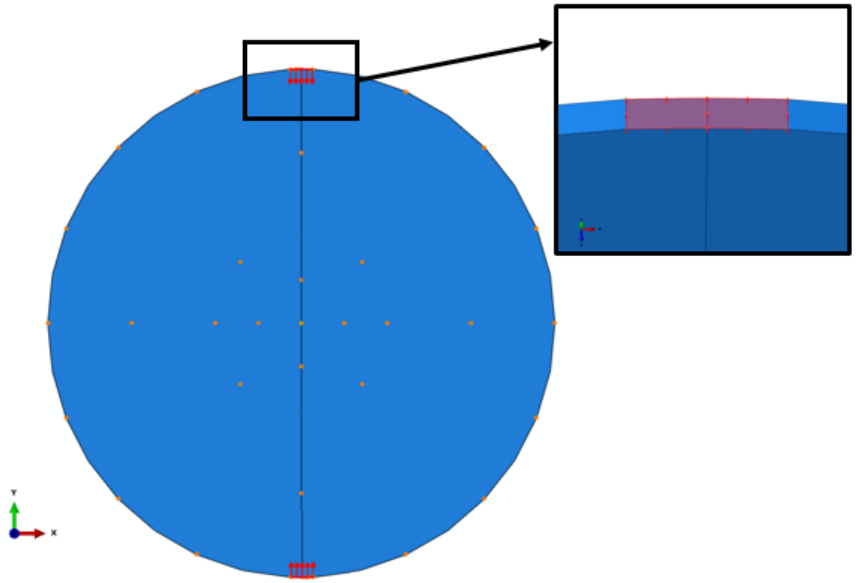

Figure 3.8: Displacement loading applied in concentric model.

Mesh is generated using 4-node linear tetrahedral elements (C3D4). Figure 3.9 shows the meshed geometry of concentric model.

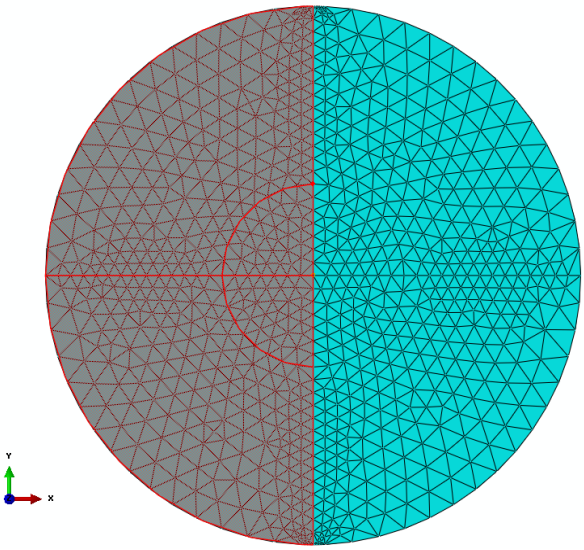

Figure 3.9: Meshed geometry of concentric model.

Additionally, the sandwich model with different interface orientations is created changing the interface orientation angle. The interface orientation angle, θ, is set as 0°, 15°, 30°, 45°, 60°, 75° and 90° rotating the disc clockwise around z-axis and keeping loading fixed along y-axis.

Table 3.4 shows the range of calculation time, number of elements, number of nodes of all finite element analyses conducted on diametral compression bond strength test on d-a interface.

FE Model	CPU Time [sec]	Number of Elements	Number of Nodes
Intact Model	454.7 – 836.2	2740	959
Concentric Model	906.1 – 6392.4	5333 - 5378	10641 - 10921
Ring Model	4995.4	4483	9111
Sandwich Model	1657 – 1877.4	5168 - 5738	1703 - 1863

Table 3.4: Calculation time, number of elements and nodes of FE Analyses

3.2 RESULTS AND DISCUSSION

The data extracted from simulations are assessed comparing interface orientations of sandwich model, varying material properties of concentric model and ring model, where the inner layer is removed with reference to concentric model, in terms of both reaction forces and displacements on the load surfaces in the loading direction, RF_2 and U_2, respectively. Moreover, contour plots are presented for all cases in terms of octahedral normal strain and octahedral shear strain, which reveal local volume change and local distortion, respectively, at the increment where each specimen reaches to failure. Failure is detected calculating the peak value of RF_2 for each case. Additionally, octahedral shear strain maps of all models are given in xy-plane fixing their scales on octahedral shear strain magnitude at which each model fails. In other words, these octahedral shear strain maps

present local distortion beyond failure for each case. Subsequently, octahedral shear strain maps of concentric models with dentin-like material and adhesive and dentin-like ring model are compared to experimental results of the study conducted by Carrera to reveal more insights about diametral compression bond strength test [5].

3.2.1 Yield Strength in Different Interface Orientations of Sandwich Model

Figure 3.10 depicts apparent tensile strength values of sandwich model at different interface orientations. Apparent tensile strength values are computed converting peak reaction forces from the numerical analysis results using the equation, $\sigma=2F/\pi Dh$, setting F as peak reaction force, D as disc diameter and h as disc thickness.

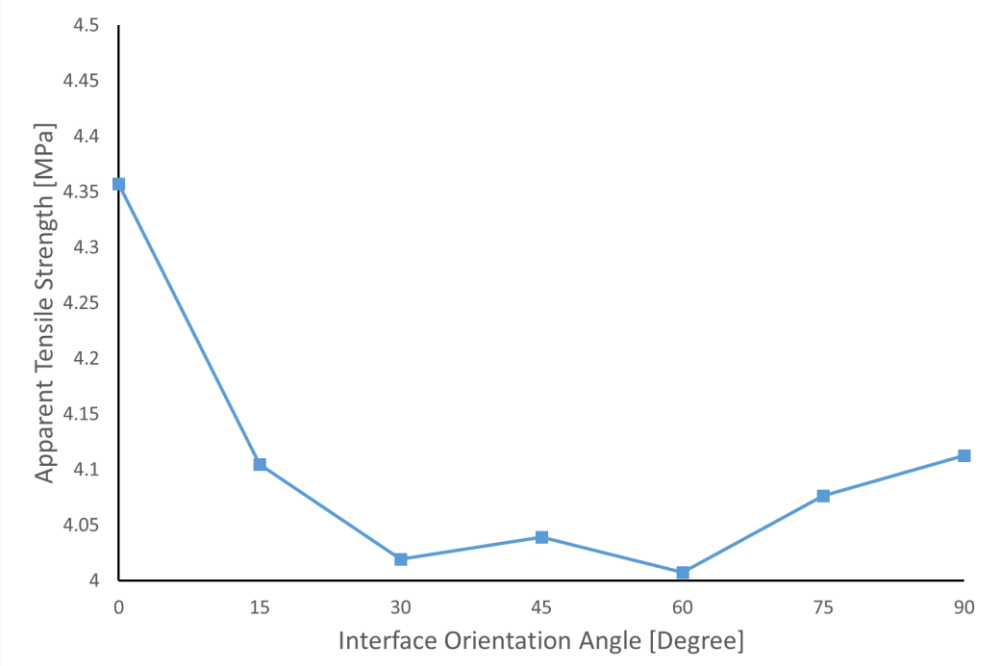

Figure 3.10: Apparent tensile strength of sandwich model at different interface orientations

As it is seen in Figure 3.10, apparent tensile strength drops changing interface orientation angle between 15° and 90° comparing with the apparent tensile strength value at 0°. In other words, sandwich model has the highest apparent tensile strength (~ 4.35 MPa), when the interface is oriented along the loading axis. Moreover, the lowest apparent tensile strength is observed when sandwich model is at interface orientation of 60°, which is ~4MPa. It is also seen that stiffness of sandwich model at interface orientation of 30° is very close to stiffness at 60°. Besides, sandwich model is stiffer at interface orientations of 15°, 75° and 90° (~4.1 MPa) than interface orientation of 60° but still has lower stiffness than interface orientation of 0°.

3.2.2 Yield Strength vs. Displacement

Figure 3.11 shows that stiffness of sandwich model at any interface orientation is lower than dentin-like intact model and higher than composite-like intact model comparing peak RF_2 values of all models. Moreover, sandwich model fails at higher RF_2 at interface orientation of 0° than any other interface orientations. It is also seen that sandwich model undergoes significant post-peak softening at interface orientations between 15° and 90° comparing with interface orientation of 0°, dentin-like and composite-like intact models.

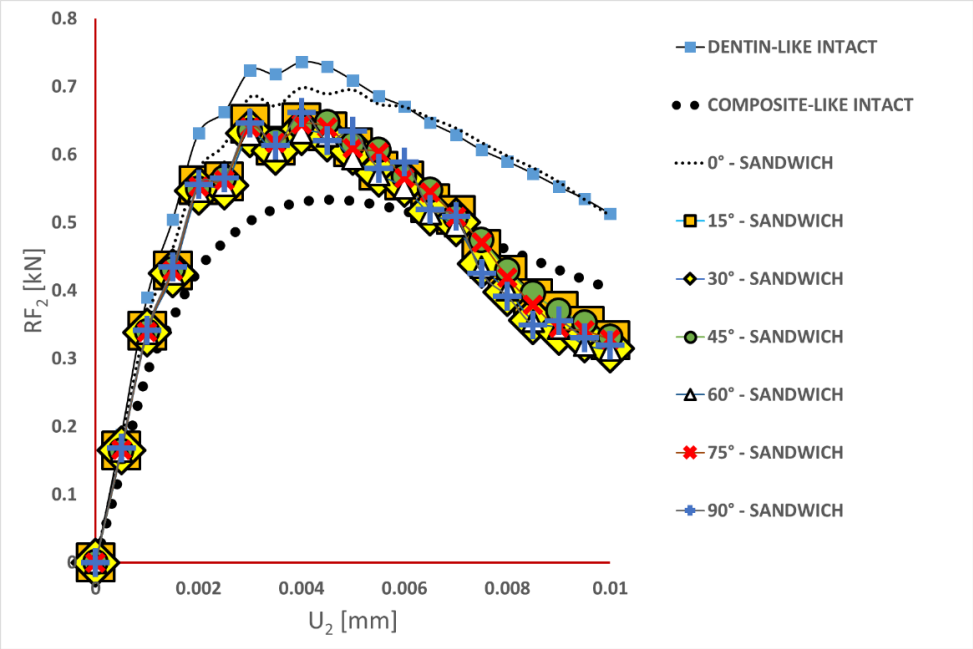

Figure 3.11: Reaction forces vs. displacement in loading direction (Sandwich model)

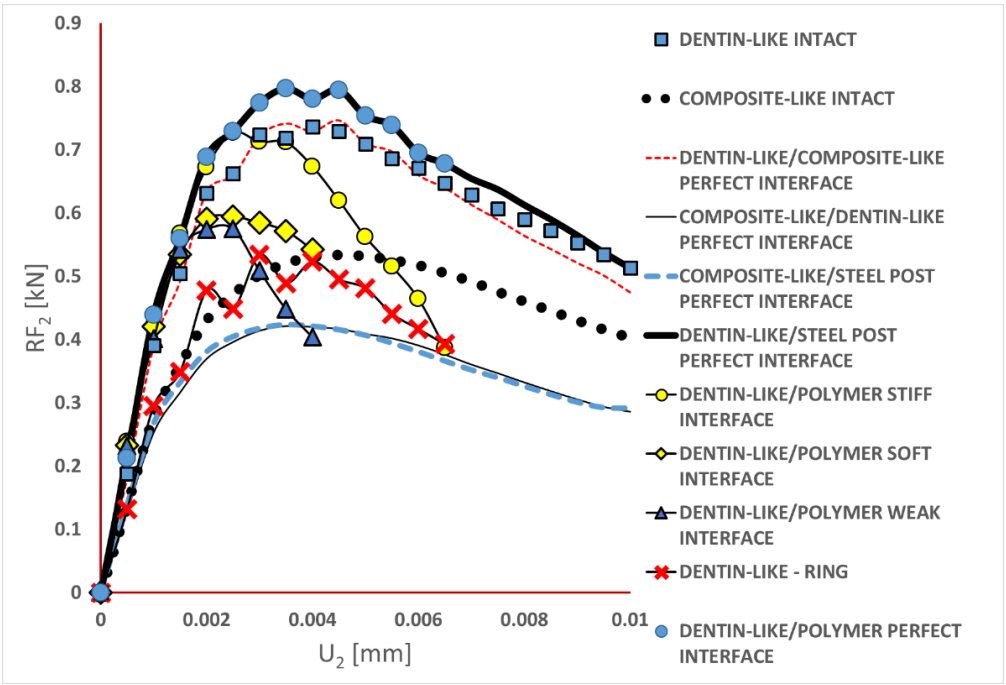

Figure 3.12: Reaction forces vs. displacement in loading direction (Concentric model)

On the other hand, Figure 3.12 represents the RF_2 results of concentric models varying in material selection and interfacial stiffness and dentin-like ring model with respect to displacement loading, U_2, comparing with dentin-like and composite like intact models. It is seen that strength of concentric model decreases when the interfacial stiffness gets lower considering models where outer layer is dentin-like material and inner layer is polymer. Interfacial stiffness decreases as perfect, stiff, soft and weak interface. Eventually, lowest strength can be considered as the ring model's strength which is also dentin-like as outer layer but inner layer is missing comparing to dentin-like/polymer concentric model. Moreover, strength of intact and concentric models are very close to each other in presence of perfect interface considering that outer layer is dentin-like and inner layer is composite-like material comparing to dentin-like intact model. However, strength of concentric model with perfect bond is significantly lower than intact model considering that outer layer is composite-like material and inner layer is either dentin-like material or steel post comparing with composite-like intact model. Besides, concentric model with perfect bond becomes stiffer than intact model considering that outer layer is dentin-like material and inner layer is either steel post or polymer comparing with dentin-like intact model.

3.2.3 Octahedral Normal Strain Maps

Figure 3.13 presents octahedral normal strain maps of concentric model with varying materials comparing to composite-like and dentin-like intact models and dentin-like ring model which reveals local volume change within the presented models.

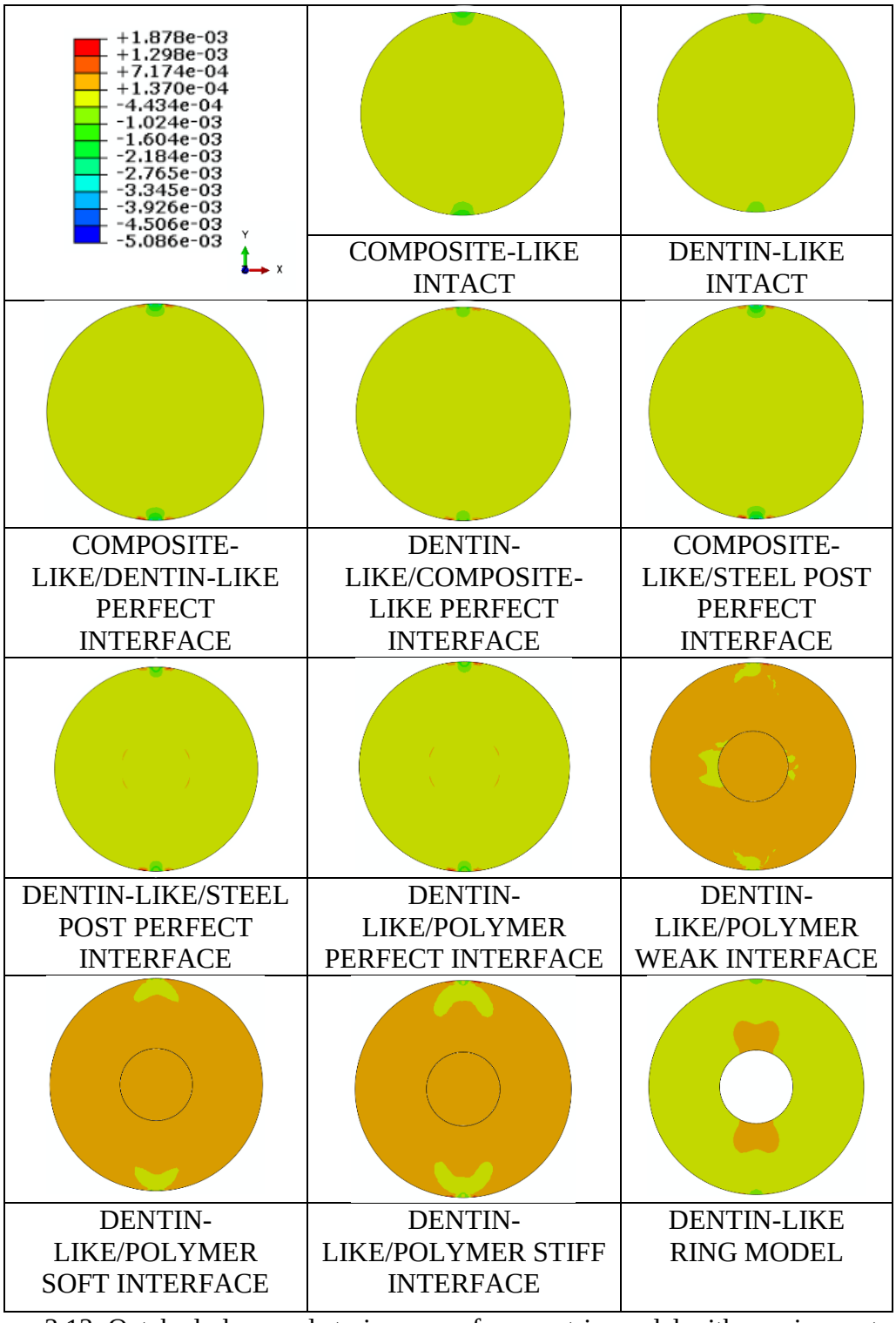

Figure 3.13: Octahedral normal strain maps of concentric model with varying materials comparing to composite-like and dentin-like intact models and dentin-like ring model

A fixed strain magnitude scale is used to create contours where each specimen reaches to its peak value of RF_2, which indicates failure. It is seen that significant shrinkage takes place around load surfaces in intact models and all concentric models with perfect interface. Additionally, the shrinkage around load surfaces of composite-like intact model is higher than concentric models with perfect interface and dentin-like intact model. It is also observed in concentric models with perfect interface that areas at the edge close to load surfaces undergo some dilation. Furthermore, shrinkage in the vicinity of load surfaces increases in concentric models where inner layer is polymer and outer layer is dentin-like material increasing stiffness of interface. Generally, dilation is significantly higher around interface within concentric models with imperfect interface than concentric model (dentin-like/polymer) with perfect interface. Particularly, weak interface create discontinuity around interface in terms of dilation. Finally, significant dilation is observed at the inner edge of dentin-like ring model in the vicinity of loading axis.

Figure 3.14 shows octahedral normal strain maps of sandwich model at different interface orientations comparing to composite-like and dentin-like intact models. Top load surface of sandwich model which is on the composite-like material's side undergoes more shrinkage than bottom load surface which is on the dentin-like material's side at interface orientations between 15° and 90°. It is also seen that sandwich model has the least shrinkage around load surfaces at interface orientation of 0° comparing with any other interface orientations between 15° and 90°.

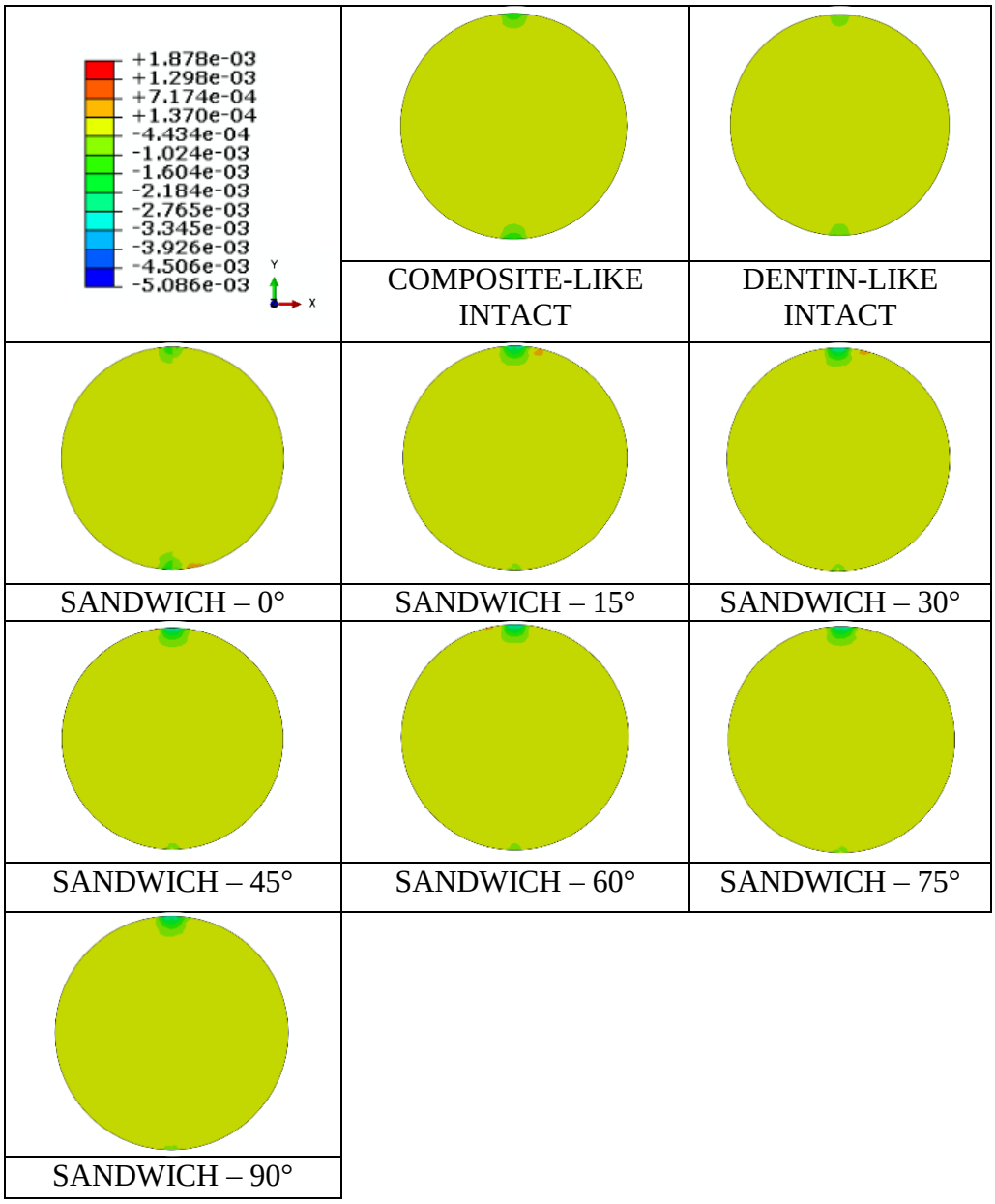

Figure 3.14: Octahedral normal strain maps of sandwich model at different interface orientations comparing to composite-like and dentin-like intact models

3.2.4 Octahedral Shear Strain Maps

Figure 3.15 shows the octahedral shear strain maps of concentric model with varying materials comparing to composite-like and dentin-like intact models and

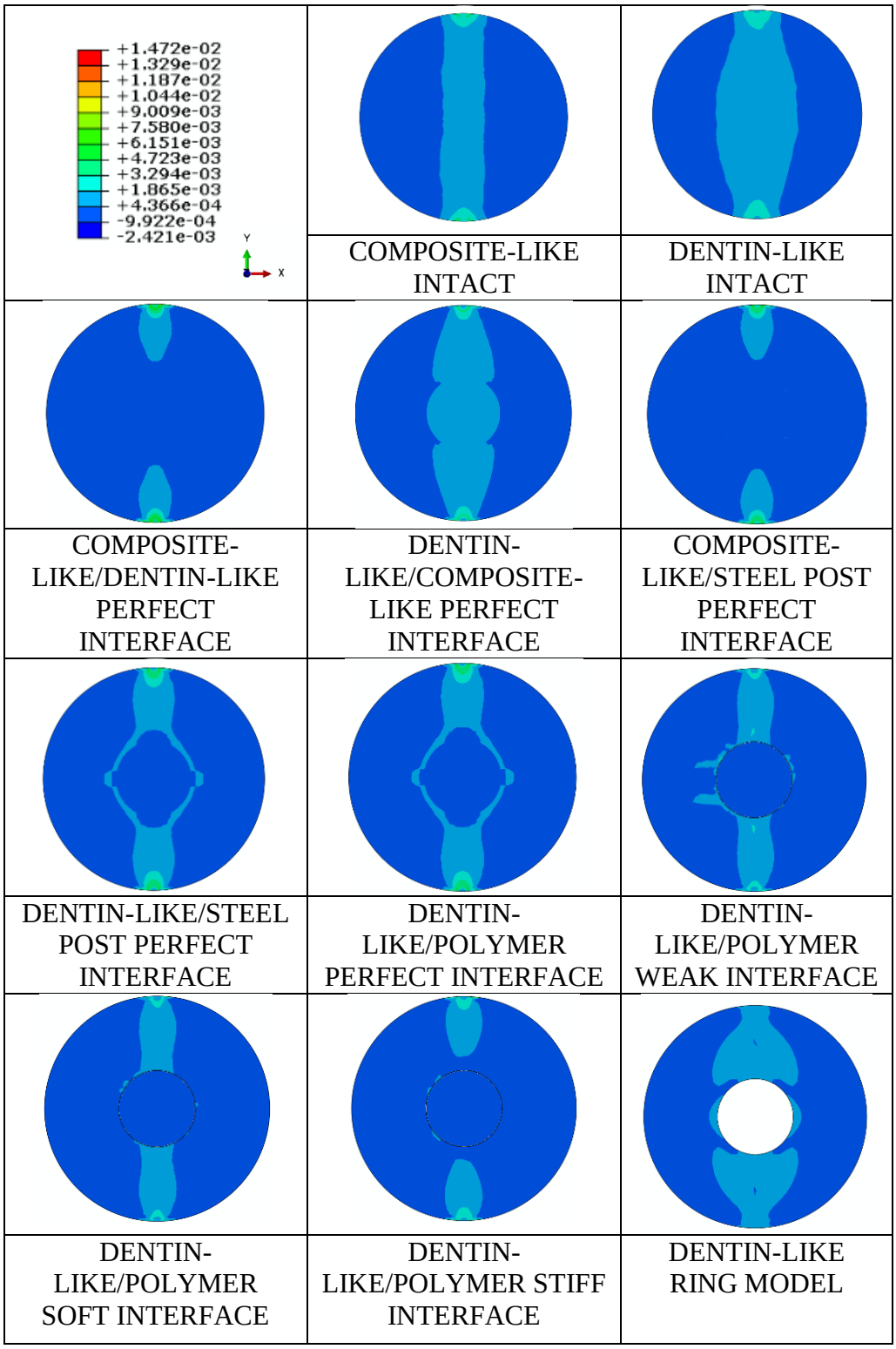

Figure 3.15: Octahedral shear strain maps of concentric model with varying materials comparing to composite-like and dentin-like intact models and dentin-like ring model

dentin-like ring model which reveals local distortion within the presented models. A fixed strain magnitude scale is used to create strain maps where each specimen reaches to its peak value of RF_2. Local distortion is significantly higher in vicinity of load surface in all concentric models with perfect interface and intact models. Local distortion is substantially higher along the loading axis in intact models, dentin-like ring model and concentric model where inner layer is composite-like and outer layer is dentin-like material. It is also observed that very high around load surfaces in all models presented except for dentin-like ring model. In other words, local distortion is concentrated close to the inner edge of ring model along its loading axis. Moreover, it is seen that local distortion along the loading axis experiences discontinuity introducing imperfection to interface comparing concentric model with perfect interface and imperfect interfaces where inner layer is polymer and outer layer is dentin-like material. Furthermore, local distortion is concentrated at load surfaces in concentric models where outer layer is composite-like material. Both composite-like and dentin-like intact models have high local distortion along their loading axis and dentin-like intact model has higher local distortion along its loading axis than composite-like intact model.

Figure 3.16 depicts octahedral shear strain maps of sandwich model at different interface orientations comparing to composite-like and dentin-like intact models. Generally, it is seen that local distortion is significantly higher around top load surfaces which are on composite-like material's side than load surfaces on dentin-like material's side. Mainly, local distortion is higher along loading axis in all models and it is observed that there is local distortion discontinuity in sandwich model at interface orientations

between 30° and 90°. Particularly, the most severe discontinuity is observed at interface orientation of 30°.

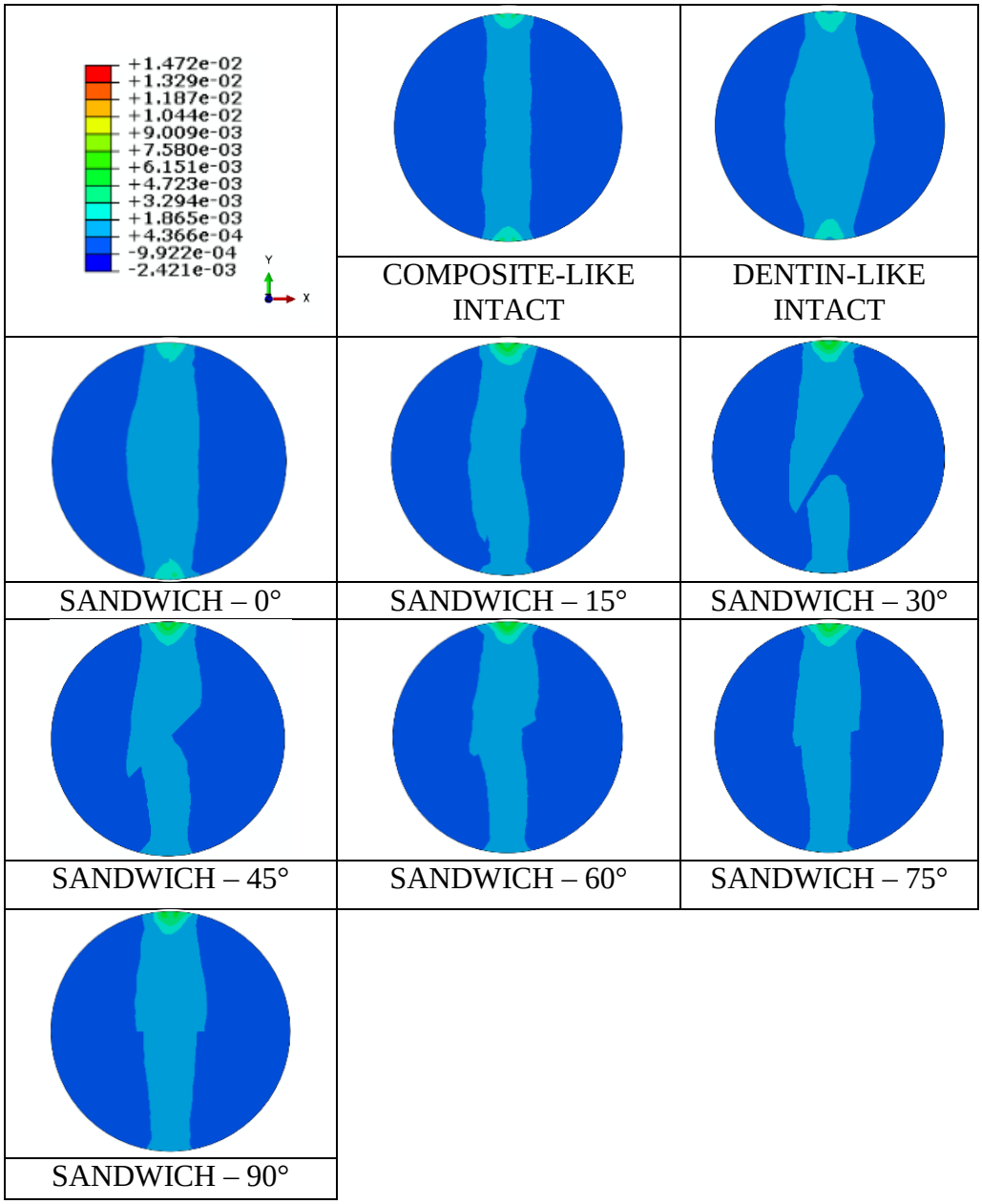

Figure 3.16: Octahedral shear strain maps of sandwich model at different interface orientations comparing to composite-like and dentin-like intact models

Figure 3.17 represents the octahedral shear strain maps of concentric model with varying materials and different interfacial stiffness comparing to composite-like and dentin-like intact models and dentin-like ring model. Octahedral shear strain magnitude

scales are fixed at values of octahedral shear strain at failure of each model and contour plots present the octahedral shear strain maps of each model beyond its failure. Furthermore, concentric models (dentin-like/polymer) with varying interface stiffness and dentin-like ring model are compared with fracture image of concentric specimen from experimental study [5]. Inner diameter of the sample in experimental study is 2 mm, outer diameter is 5 mm and disc thickness is 2 mm. Outer layer of specimen is dentin extracted from bovine incisor and inner layer is applied as resin composite. The following discussion is conducted considering that grey area indicates local distortion beyond each models failure which can be taken as indication of fracture. Local distortion is significantly high along loading axis of intact models and concentric model with perfect interface where outer layer is dentin-like and inner layer is composite-like material beyond their failure. On the other hand, local distortion beyond failure is substantially high only in close vicinity of load surfaces in concentric models with perfect interface where outer layer is composite-like material.

Results of ring model and concentric model with various interface properties, where outer layer is dentin-like material and inner layer is polymer, enable to comprehensively study insights of experimental study. According to the experimental study, debonding happens at the interface first and then, fracture evolves from inner edge to outer edge of dentin along loading axis (Figure 3.18) [5]. Dentin-like ring model shows that local distortion beyond failure is concentrated starting from the inner edge where dentin-like ring model is considered as post-debonding case since there is neither inner layer nor interface involved.

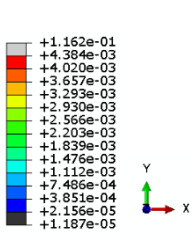

COMPOSITE-LIKE INTACT

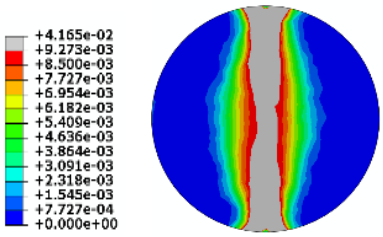

DENTIN-LIKE INTACT

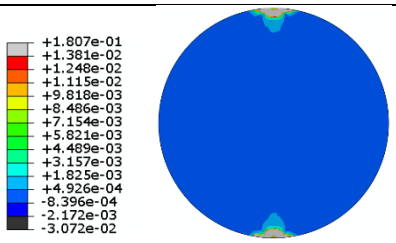

COMPOSITE-LIKE/DENTIN-LIKE PERFECT INTERFACE

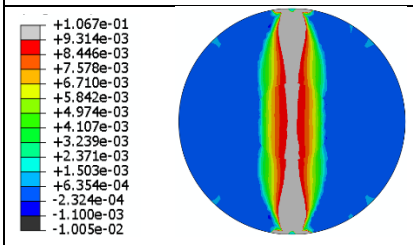

DENTIN-LIKE/COMPOSITE-LIKE PERFECT INTERFACE

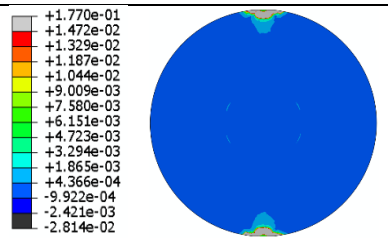

COMPOSITE-LIKE/STEEL POST PERFECT INTERFACE

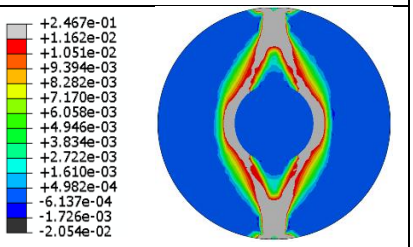

DENTIN-LIKE/STEEL POST PERFECT INTERFACE

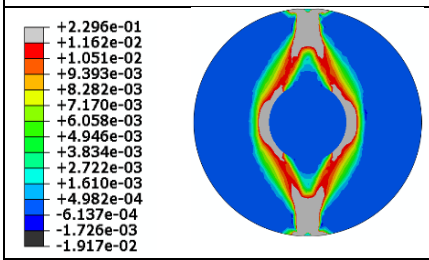

DENTIN-LIKE/POLYMER PERFECT INTERFACE

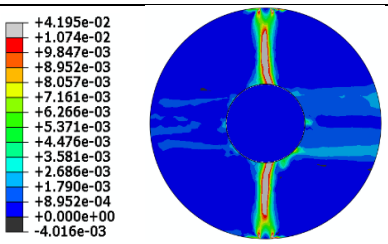

DENTIN-LIKE/POLYMER WEAK INTERFACE

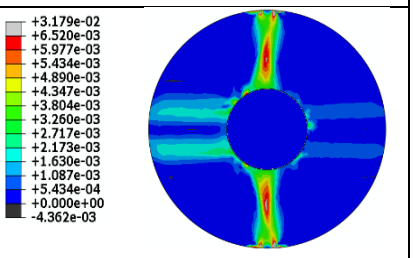

DENTIN-LIKE/POLYMER SOFT INTERFACE

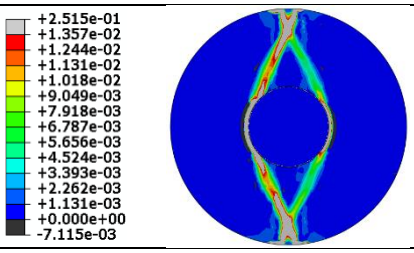

DENTIN-LIKE/POLYMER STIFF INTERFACE

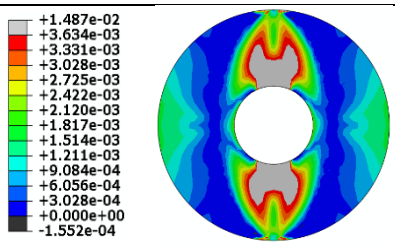

DENTIN-LIKE RING MODEL

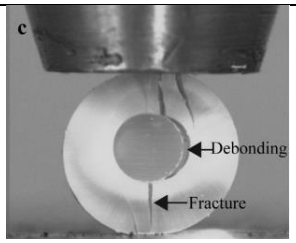

DENTIN-POLYMER FRACTURE PATTERN FROM EXPERIMENT [5]

Figure 3.17: Octahedral shear strain maps of concentric model with varying materials and different interfacial stiffness comparing to composite-like and dentin-like intact models, dentin-like ring model and fracture pattern from experiment [5]

On the other hand, local distortion reaches beyond failure starting from load surface along loading axis and at interface in concentric model with perfect interface where outer layer is dentin-like material and inner layer is polymer. Areas where local distortion reaches beyond failure vary changing stiffness of interface in the aforementioned model. The heavily distorted area follows the path from load surface to distorted area at the interface instead of loading axis when model is with stiff interface. The model with weak interface experiences heavy distortion along loading axis between interface and some location away from load surface. Finally, the model with soft interface undergoes high distortion along loading axis neither inner edge nor outer edge but almost in the middle of dentin-like layer.

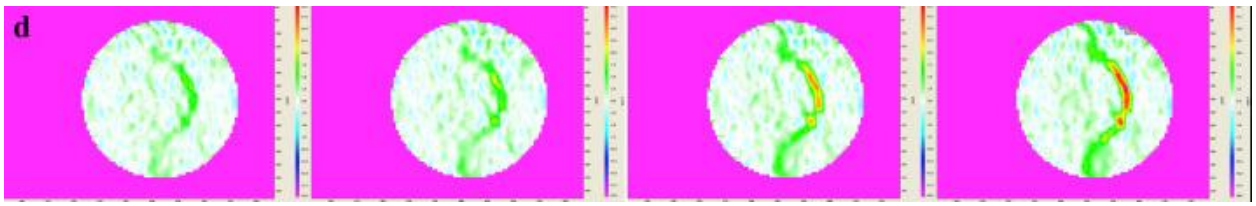

Figure 3.18: Digital image correlation results from experiment where the evolution of strain concentrations is presented [5]

Figure 3.19 depicts octahedral shear strain maps of sandwich model at different interface orientations comparing to composite-like and dentin-like intact models. Octahedral shear strain magnitude scales are fixed according to failure octahedral shear strain values of each model. Local distortion beyond failure is observed along loading axis but only in composite-like material's side when sandwich model is at interface orientations of 15° and 30°. On the other hand heavily distorted area starts from load surface on composite-like material's side and passes through interface along loading axis when sandwich model is oriented between 45° and 90°. Moreover, discontinuity in local distortion is observed in dentin-like material's side along loading axis when sandwich

model is at interface orientation of 0°. Additionally, sandwich model follows the same local distortion pattern beyond failure at interface orientation of 0° as dentin-like intact model.

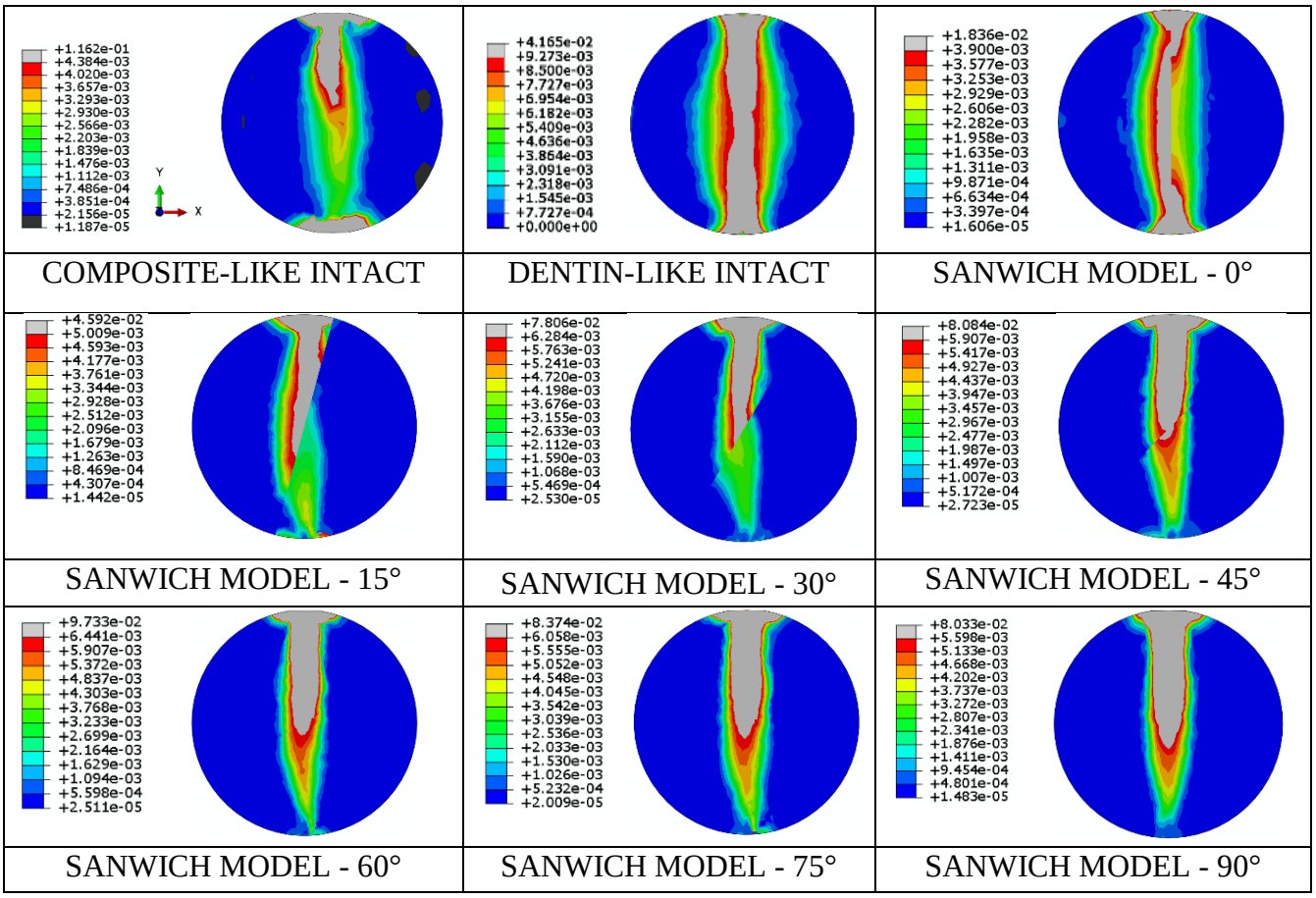

Figure 3.19: Octahedral shear strain maps of sandwich model at different interface orientations comparing to composite-like and dentin-like intact models

3.2.5 Diametral Expansion vs. Displacement

Diametral expansion data is processed as it is explained in Section 2.3.5. Results are plotted taking related cases into account in order to carry out a reliable assessment. In other words, sandwich model at varying interface orientations is compared with dentin-like and composite-like intact models. Moreover, concentric model with varying materials and interface stiffness is compared with dentin-like ring and intact models. Mainly, it is

observed that all models nonlinearly increase diametral expansion Figure 3.20 and Figure 3.21. Sandwich model has lower diametral expansion than dentin-like intact model but higher than composite-like intact model at any interface orientation Figure 3.20. Additionally, highest diametral expansion takes place when sandwich model is oriented along loading axis whereas all other interface orientations results in approximately the same amount of diametral expansion.

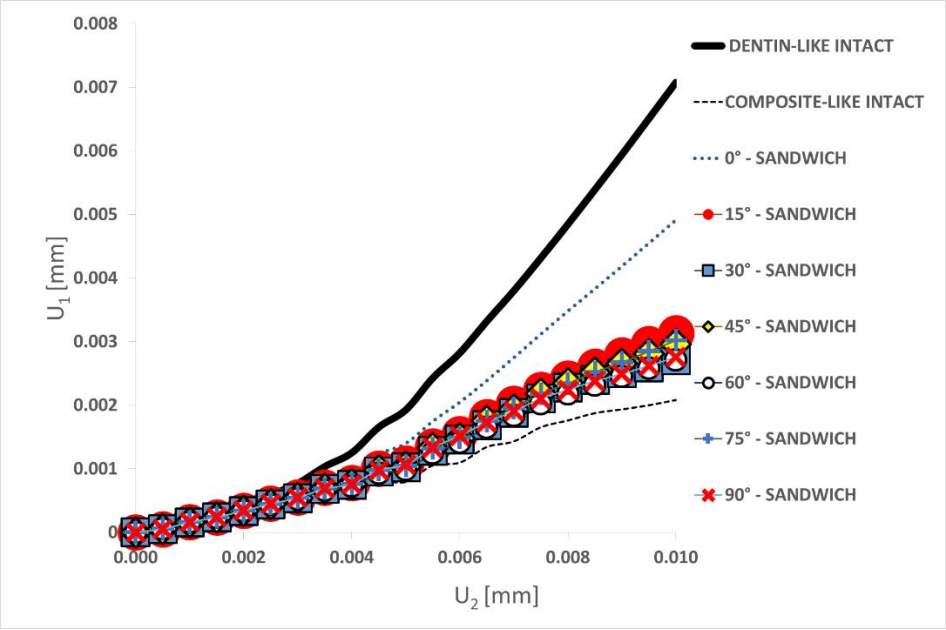

Figure 3.20: Diametral expansion results of sandwich model at different interface orientations comparing to composite-like and dentin-like intact models

Figure 3.21 shows that dentin-like ring experiences significantly higher diametral expansion comparing with any other model due to flaw (hollow structure) within the disc. Particularly, it is observed that concentric model with weak interface expands highly nonlinearly on diametral axis when outer layer is dentin-like material and inner layer is polymer. The least diametral expansion is seen when outer layer of concentric model with perfect interface is composite-like material and changing inner layer as either steel post or dentin-like does not provide any observable significance in terms of diametral expansion.

Accordingly, it is seen that concentric model with perfect interface undergoes almost the same amount of diametral expansion when outer layer is dentin-like material and varying inner layer as either steel post or polymer does not provide any substantial change in diametral expansion. Finally, it is observed that concentric model expands more in x-axis decreasing interface stiffness when outer layer is dentin-like material and inner layer is polymer.

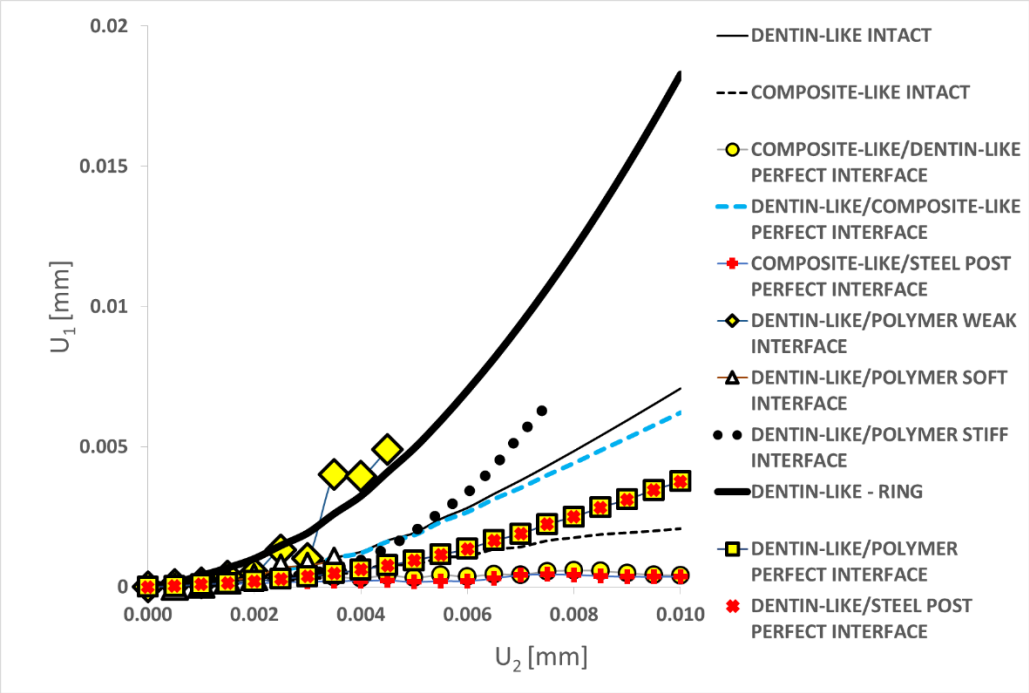

Figure 3.21: Diametral expansion results of concentric model with varying materials comparing to composite-like and dentin-like intact models and dentin-like ring model

CHAPTER 4

SUMMARY, CONCLUSION AND FUTURE WORK

4.1 SUMMARY AND CONCLUSION

This study presents implementation of a user-defined nonlinear material model into a commercial finite element analysis software to investigate more insights about indirect tensile test and diametral compression bond strength test. Finite element analysis results are compared to experimental results to show the predicting capability of nonlinear material model where the analysis is conducted on indirect tensile test on concrete disc specimens. Afterwards, finite element analysis is conducted on dentin-adhesive interface using varying materials on different models such as intact, concentric, ring and sandwich models changing interface stiffness and interface orientations.

Prediction capability of generated models is convincing looking at results such as local distortion beyond failure comparing to experimental fracture patterns of indirect tensile test on concrete samples. Results show that models are able to capture the failure phenomena and fracture evolution very close to experimental results.

The results of finite element analysis on indirect tensile test also show that the failure can be controlled to become either as a tensile or a shear failure by introducing a flaw within the specimen and changing the flaw orientation between 15° and 75°.

Accordingly, finite element analysis conducted on diametral compression bond strength test on dentin-adhesive interface provides more insights about test application and further improvement about the test procedure.

It is seen from the analysis carried out on sandwich model, changing the interface orientations enable to measure different bond strength such as tensile and shear bond strength. Diametral expansion leads specimen to tensile failure when sandwich model's interface is oriented along loading axis where the normal of interface plane matches diametral axis. Furthermore, shear failure of interface is observed changing interface orientation away from loading axis. Consequently, design of diametral compression test on sandwich model allows both bond tensile and bond shear strength test changing interface orientation.

Moreover, the main focus of bond strength test is measurement of exact distortion which would create debonding exactly at the interface. In other words, premature failure of any of the components creating interface leads to underestimating real bond strength at the interface. Accordingly, finite element analysis carried out on d-a interface shows that potential further factors, such as thickness selection of the outer layer in concentric model, can lead to more accurate results where initial failure can be shifted to interface and accurate bond strength can be measured.

4.2 FUTURE WORK

In this present work, the abovementioned outer layer's thickness effect has not been investigated. It needs to be investigated in the future to understand the effect of outer layer's thickness on debonding at interface in concentric model conducting more parametric

studies varying outer layer's thickness. Furthermore, sandwich model is created using only dentin-like and composite-like materials and also, only with perfect interface. To establish better understanding on diametral compression bond strength test on sandwich model, further analysis is needed assigning varying material properties and imperfect interface. Finally, accuracy of debonding analysis in all models needs to be improved using interface properties close to experimental conditions. This study uses linear interface properties and perfect interface which is not possible in real life. The accuracy can be improved introducing damage to interface and allowing separation at interface in all models. Finally, physical experiments need to be conducted after designing experiments according to predictions of numerical results.

BIBLIOGRAPHY

[1] T. Beazoglou, S. Eklund, D. Heffley, J. Meiers, L.J. Brown, H. Bailit, Economic impact of regulating the use of amalgam restorations, Public Health Rep 122(5) (2007) 657-63.

[2] R.E. Bogacki, R.J. Hunt, M. del Aguila, W.R. Smith, Survival analysis of posterior restorations using an insurance claims database, Oper Dent 27(5) (2002) 488-92.

[3] P.E. Murray, L.J. Windsor, T.W. Smyth, A.A. Hafez, C.F. Cox, Analysis of pulpal reactions to restorative procedures, materials, pulp capping, and future therapies, Crit Rev Oral Biol Med 13(6) (2002) 509-20.

[4] J.P. Van Nieuwenhuysen, W. D'Hoore, J. Carvalho, V. Qvist, Long-term evaluation of extensive restorations in permanent teeth, J Dent 31(6) (2003) 395-405.

[5] C.A. Carrera, Y.C. Chen, Y. Li, J. Rudney, C. Aparicio, A. Fok, Dentin-composite bond strength measurement using the Brazilian disk test, J Dent 52 (2016) 37-44.

[6] N.Y. Cho, J.L. Ferracane, I.B. Lee, Acoustic Emission Analysis of Tooth-Composite Interfacial Debonding, Journal of Dental Research 92(1) (2013) 76-81.

[7] Y. An, D. Li, N. Roohpour, J.E. Gautrot, A.H. Barber, Failure mechanisms in denture adhesives, Dent Mater 32(5) (2016) 615-23.

[8] A. Misra, P. Spencer, O. Marangos, Y. Wang, J.L. Katz, Parametric study of the effect of phase anisotropy on the micromechanical behaviour of dentin-adhesive interfaces, J R Soc Interface 2(3) (2005) 145-57.

[9] V. Singh, A. Misra, O. Marangos, J. Park, Q. Ye, S.L. Kieweg, P. Spencer, Fatigue life prediction of dentin-adhesive interface using micromechanical stress analysis, Dent Mater 27(9) (2011) e187-95.

[10] P. Spencer, Q. Ye, J. Park, E.M. Topp, A. Misra, O. Marangos, Y. Wang, B.S. Bohaty, V. Singh, F. Sene, J. Eslick, K. Camarda, J.L. Katz, Adhesive/Dentin interface: the weak link in the composite restoration, Ann Biomed Eng 38(6) (2010) 1989-2003.

[11] S.J. Marshall, S.C. Bayne, R. Baier, A.P. Tomsia, G.W. Marshall, A review of adhesion science, Dent Mater 26(2) (2010) e11-6.

[12] J.P. Matinlinna, L.V. Lassila, I. Kangasniemi, A. Yli-Urpo, P.K. Vallittu, Shear bond strength of Bis-GMA resin and methacrylated dendrimer resins on silanized titanium substrate, Dent Mater 21(3) (2005) 287-96.

[13] P.E. Cardoso, R.R. Braga, M.R. Carrilho, Evaluation of micro-tensile, shear and tensile tests determining the bond strength of three adhesive systems, Dent Mater 14(6) (1998) 394-8.

[14] N. Kanemura, H. Sano, J. Tagami, Tensile bond strength to and SEM evaluation of ground and intact enamel surfaces, J Dent 27(7) (1999) 523-30.

[15] S.R. Armstrong, D.B. Boyer, J.C. Keller, Microtensile bond strength testing and failure analysis of two dentin adhesives, Dent Mater 14(1) (1998) 44-50.

[16] J.M. Patierno, F.A. Rueggeberg, R.W. Anderson, R.N. Weller, D.H. Pashley, Push-out strength and SEM evaluation of resin composite bonded to internal cervical dentin, Endod Dent Traumatol 12(5) (1996) 227-36.

[17] L. De Lorenzis, A. Rizzo, A. La Tegola, A modified pull-out test for bond of near-surface mounted FRP rods in concrete, Compos Part B-Eng 33(8) (2002) 589-603.

[18] Y. Shimada, S. Yamaguchi, J. Tagami, Micro-shear bond strength of dual-cured resin cement to glass ceramics, Dental Materials 18(5) (2002) 380-388.

[19] A. Hashimoto, H. Ohno, M. Kaga, H. Sano, F.R. Tay, H. Oguchi, Y. Araki, M. Kubota, Over-etching effects on micro-tensile bond strength and failure patterns for two dentin bonding systems, Journal of Dentistry 30(2-3) (2002) 99-105.

[20] S.S. Scherrer, P.F. Cesar, M.V. Swain, Direct comparison of the bond strength results of the different test methods: a critical literature review, Dent Mater 26(2) (2010) e78-93.

[21] S. Phrukkanon, M.F. Burrow, M.J. Tyas, Effect of cross-sectional surface area on bond strengths between resin and dentin, Dent Mater 14(2) (1998) 120-8.

[22] S. Armstrong, S. Geraldeli, R. Maia, L.H. Raposo, C.J. Soares, J. Yamagawa, Adhesion to tooth structure: a critical review of "micro" bond strength test methods, Dent Mater 26(2) (2010) e50-62.

[23] J.H. Ye, F.Q. Wu, J.Z. Sun, Estimation of the tensile elastic modulus using Brazilian disc by applying diametrically opposed concentrated loads, Int J Rock Mech Min 46(3) (2009) 568-576.

[24] D. Zaytsev, P. Panfilov, Deformation behavior of human dentin in liquid nitrogen: a diametral compression test, Mater Sci Eng C Mater Biol Appl 42 (2014) 48-51.

[25] F. Carneiro, A. Barcellos, Concrete tensile strength, Union of testing and research laboratories for materials and structures 13 (1953).

[26] D.Y. Li, L.N.Y. Wong, The Brazilian Disc Test for Rock Mechanics Applications: Review and New Insights, Rock Mech Rock Eng 46(2) (2013) 269-287.

[27] E.M.R. Fairbairn, F.J. Ulm, A tribute to Fernando L. L. B. Carneiro (1913-2001) - Engineer and scientist who invented the Brazilian test, Mater Struct 35(247) (2002) 195-196.

[28] B. Ramanathan, V. Raman, Split tensile strength of cohesive soils, Soils and Foundations 14(1) (1974) 71-76.

[29] Standard Test Method for Splitting Tensile Strength of Intact Rock Core Specimens, ASTM International, 2016.

[30] Standard Test Method for Splitting Tensile Strength of Cylindrical Concrete Specimens, ASTM International, 2004.

[31] P. Jonsen, H.A. Haggblad, K. Sommer, Tensile strength and fracture energy of pressed metal powder by diametral compression test, Powder Technol 176(2-3) (2007) 148-155.

[32] C. Shang, I.C. Sinka, J. Pan, Modelling of the break force of tablets under diametrical compression, Int J Pharmaceut 445(1-2) (2013) 99-107.

[33] D. Zaytsev, P. Panfilov, Deformation behavior of human enamel under diametral compression, Mater Lett 136 (2014) 130-132.

[34] S.H. Huang, L.S. Lin, J. Rudney, R. Jones, C. Aparicio, C.P. Lin, A. Fok, A novel dentin bond strength measurement technique using a composite disk in diametral compression, Acta Biomater 8(4) (2012) 1597-602.

[35] S.-H. Huang, L.-S. Lin, A.S.L. Fok, C.-P. Lin, Diametral compression test with composite disk for dentin bond strength measurement – Finite element analysis, Dental Materials 28(10) (2012) 1098-1104.

[36] Y. Li, C. Carrera, R. Chen, J. Li, Y. Chen, P. Lenton, J.D. Rudney, R.S. Jones, C. Aparicio, A. Fok, Fatigue failure of dentin–composite disks subjected to cyclic diametral compression, Dental Materials 31(7) (2015) 778-788.

[37] A. Pérez-González, J.L. Iserte-Vilar, C. González-Lluch, Interpreting finite element results for brittle materials in endodontic restorations, BioMedical Engineering OnLine 10(1) (2011) 44.

[38] A. Misra, V. Singh, R. Parthasarathy, Material-tissue interfacial phenomena: challenges in mathematical modeling, Material-Tissue Interfacial Phenomena: Contributions from Dental and Craniofacial Reconstructions (2016) 253.

[39] P. Poorsolhjouy, A. Misra, Effect of intermediate principal stress and loading-path on failure of cementitious materials using granular micromechanics, Int J Solids Struct 108 (2017) 139-152.